Science of Remote Sensing 13 (2026) 100452

Contents lists available at ScienceDirect

Science of Remote Sensing

journal homepage: www.sciencedirect.com/journal/science-of-remote-sensing

Soil moisture retrievals under crops using compact polarimetric surface scattering and vegetation radiative transfer models

Bhanu Prakash Mookkuthala Erkaramana [a,*], Kalifa Goïta [a], Ramata Magagi [a], Anke Fluhrer [b], Florian Hellwig [c,b], Tanya Copley [d], Thomas Jagdhuber [b,c]

[a] Centre d'applications et de recherches en télédétection (CARTEL), Université de Sherbrooke, Québec, Canada
[b] Microwaves and Radar Institute, German Aerospace Center, Wessling, Germany
[c] Institute of Geography, Augsburg University, Augsburg, Germany
[d] Centre de recherche sur les grains (CÉROM), Saint-Mathieu-de-Beloeil, Québec, Canada

ARTICLE INFO

Keywords:
Synthetic aperture radar (SAR)
Compact polarimetry (CP)
Soil moisture
Agricultural fields
Crops
Retrieval algorithms
CP-Advanced integral equation model (CP-AIEM)
Water cloud model (WCM)
Vegetation single scattering radiative transfer (SSRT)
Validation

ABSTRACT

Accurate soil moisture estimation from Synthetic Aperture Radar (SAR) observations under crop growth conditions is challenging because of the complexity of extracting the soil contributions from the total backscatter. Compact Polarimetric (CP) SAR with reduced design requirements represents a viable alternative to fully polarimetric SAR but remains underutilized. The study introduces two soil moisture retrieval algorithms using the canopy Water Cloud Model (WCM) and vegetation Single Scattering Radiative Transfer (SSRT) applied to C-band CP data. Both models are calibrated with the CP-Advanced Integral Equation Model (CP-AIEM). The proposed algorithms, i.e., CP-AIEM-WCM and CP-AIEM-SSRT, are applied to RADARSAT Constellation Mission (RCM) CP data acquired over crop fields of AAFC-Lennoxville, Estrie (2022 and 2023) and in the Montérégie (2024), in Québec (Canada). Soil moisture retrievals from soybean, corn and wheat fields perform better for lower ($\leq 30^{\circ}$) compared to higher incidence angles ($>30^{\circ}$) in terms of root-mean-square error (RMSE) (0.06–0.08 vs 0.09–0.10 m^3/m^3) and inversion rate (IR) (70–89 vs 30–60%). Among study crops, corn fields yield estimates with higher accuracy compared to soybean and wheat, with the lowest RMSE (0.06 m^3/m^3) under low incidence angle observations. Site-specific cross-validation was performed by splitting training and testing datasets to evaluate transferability of the algorithms. We observed that both algorithms perform well with similar RMSE at all incidence angles and crop type cases, with slight reduction (5–20%) in IR under cross-validation, thereby supporting the hypothesis of spatial transferability.

1. Introduction

Soil moisture plays a vital role in hydrology and climatology by influencing weather, plant growth and runoff, making its distribution important for mitigating environmental disturbances (Kornelsen and Coulibaly, 2013; Wang and Qu, 2009; Jackson et al., 1996; McNairn et al., 2012). In terms of agriculture, soil moisture influences crop growth and yield. Its accurate estimation helps to optimize irrigation scheduling and facilitate precision farming. Soil moisture is an essential climate variable affecting both regional water balance and agricultural sustainability (Verhoest et al., 2008; Joseph et al., 2008; Kim and Van Zyl, 2009). For over three decades, remote sensing using Synthetic Aperture Radar (SAR) has remained a focus of active research on surface soil moisture retrieval in agricultural lands due to its all-weather capability, independence from sunlight, penetration through vegetation cover, and high spatial resolution (Kornelsen and Coulibaly, 2013; Attema and Ulaby, 1978; Schmugge, 1983). Unlike spaceborne passive microwave methods, SAR-based approach directly retrieves soil moisture at the scale of individual crop fields (Meng et al., 2024). Characterization of soil under vegetated conditions is a complex process, given that it involves decoupling backscatter intrinsic to the soil (Balenzano et al., 2011) and the components that are related to vegetation. Substantial efforts have been undertaken by previous studies to overcome the challenges of retrieving soil moisture under vegetation cover (Mandal et al., 2021; Ulaby et al., 2014; Steele-Dunne et al., 2017). Radar backscatter is influenced by soil surface roughness, water content, and textural composition, and by several variables that are related to crop (type, phenology, distribution, water content, shape and

* Corresponding author.
E-mail address: Bhanu.Prakash.M.E@USherbrooke.ca (B.P.M. Erkaramana).

https://doi.org/10.1016/j.srs.2026.100452
Received 18 February 2026; Received in revised form 5 June 2026; Accepted 11 June 2026
Available online 13 June 2026

orientation) (Bindlish and Barros, 2001). Microwave response incurred by this soil-vegetation system depends upon the penetration capability of the SAR signals, which in turn is a function of its acquisition variables (wavelength, incidence angle), and the bio-geophysical characteristics of vegetation (water content, type, structure and density) (Liu et al., 2019). Characterizing the vegetation and its contribution to total backscatter is key to the accurate retrieval of soil parameters from radar measurements (Chauhan, 1997). Vegetation radiative transfer models help to model the canopy as randomly oriented discrete scatterers with homogeneous dielectric properties and size, relatively to the wavelength of the radar's signal (Ulaby et al., 2014).

Several past and current SAR missions have operated at various wavelengths (L-, C-, S-, X-band), polarization modes (single, dual, full, and compact polarimetry), and spatio-temporal resolutions (Moreira et al., 2013; Canada Centre for Remote Sensing, 2005). Full polarimetric (FP) SARs are usually employed by virtue of the richness of polarimetric information that they provide. However, SAR compact polarimetry (CP) is gaining attention due to its low cost to swath width ratio and high temporal resolution without much trading off polarimetric information (Raney, 2006, 2007a, 2019; Charbonneau et al., 2010; Cloude et al., 2012). CP SAR architecture consists of a single circular polarization transmission and two orthogonal polarization receptions (Raney, 2007b), which avoids time multiplexing in transmission and offers twice the swath width of FP SAR (Charbonneau et al., 2010). CP SAR was first implemented on an Earth observation satellite with India's Radar Imaging Satellite (RISAT-1), which was launched in 2012 (Chirakkal et al., 2017). The RADARSAT Constellation Mission (RCM), which was launched in 2019 by the Canadian Space Agency (CSA), is currently the only C-band CP SAR in operation. CP delivers near-accurate results comparable to the FP system (Lavalle, 2009; Brisco et al., 2013), yet relatively few CP-based techniques have been developed for agricultural parameter estimation (Raney, 2021). Despite its strong potential and practical advantages, this area remains underexplored compared to traditional FP approaches.

Polarimetric decompositions such as m-δ (Raney, 2007b), m-χ (Raney et al., 2012), Random and Oriented Volume over Ground (RVoG and OVoG), and Entropy/Alpha (Cloude et al., 2012) have been developed for CP to distinguish between the scattering power of microwave responses of soil and vegetation. The polarimetric soil scattering angle (α_s) is reported to be suitable for soil moisture retrievals from C-band CP SAR data under vegetated soil conditions (Ponnurangam et al., 2016). Yet, this model does not apply to highly oriented vegetation. Empirical equations were used to incorporate the Integral Equation Model (IEM) for CP data to retrieve soil moisture under bare soil conditions (Merzouki et al., 2019a). The validity of these equations under vegetation cover has yet to be confirmed. Recently, a change-detection technique was applied to RCM time-series data to retrieve soil moisture during soybean growth (Zhou et al., 2025a). Furthermore, several studies have been conducted using machine learning and deep learning-based models for the estimation of soil parameters from CP SAR data (Zakharov et al., 2024; Dabboor et al., 2024). A polarimetric two-scale model was introduced to estimate soil moisture from CP data over bare soil (Di et al., 2024). The Modified Water Cloud Model (MWCM) (Yang et al., 2016) was calibrated for simulated CP data to retrieve soil moisture from rice fields (Mandal et al., 2021). The well-known higher-order radiative transfer model Michigan Microwave Canopy Scattering (MIMICS) (Mcdonald et al., 1990; Liang et al., 2004; Tour et al., 1994) and its simplified semi-empirical version, which is known as the Single Scattering Radiative Transform (SSRT) (De Roo et al., 2001; Liu et al., 2022), have been successfully implemented in forest and agriculture studies with FP SAR. In summary, most existing CP-based soil moisture retrieval algorithms have been developed from CP decompositions, machine learning, and time-series methods (Wang et al., 2023a). However, modelling the CP SAR backscatter interactions of soil and vegetation for agricultural parameter retrievals is comparatively less extensively explored. Thus, the motivation of this study is to develop radiative transfer models for CP backscatter returns from soil under vegetation cover in order to retrieve soil moisture.

This research builds on our previous study (Mookkuthala Erkaramana et al., 2026), where we developed the CP-Advanced Integral Equation Model (CP-AIEM) to characterize the scattering response from rough bare soil. In the current paper, we introduce two new soil moisture retrieval CP SAR approaches under crop cover conditions by empirically calibrating radiative transfer models. In the first approach, referred to as CP-AIEM-WCM, we calibrate the WCM (Attema and Ulaby, 1978) for CP observations with CP Radar Vegetation Index (CpRVI) (Mandal et al., 2020a) to characterize crop growth and to quantify the canopy contribution. Multiple scattering terms are ignored within the WCM, with CpRVI quantifying only the volume scattering term. In the second approach, which denoted CP-AIEM-SSRT, we calibrate the vegetation SSRT (De Roo et al., 2001) for CP observations with *in-situ* vegetation water content (VWC) and vegetation height (H) to quantify the vegetation contribution to total backscatter. Due to the model complexity, the volume scattering term of SSRT is calculated directly using *in-situ* VWC and H measurements. Both WCM and SSRT require soil backscattering coefficients from CP-AIEM to optimize the model parameters. The calibrated WCM and SSRT with these optimized parameters are used for the inversion of RCM CP backscatter to retrieve direct backscattering from soil. Further, CP-AIEM is inverted using a Look-up Table (LUT)-based two-parameter inversion approach (Ponnurangam et al., 2016; Merzouki et al., 2019b) to calculate the dielectric permittivity (ε), followed by Dobson's model (Dobson et al., 1985) conversion for soil moisture retrievals.

The main contribution of this research is the development of two new soil moisture retrieval algorithms (CP-AIEM-WCM and CP-AIEM-SSRT), which are dedicated to CP data. The models are calibrated and validated with the RCM CP SAR data that were acquired over different agriculture fields located in Lennoxville (Sherbrooke, Estrie) and Montérégie sites of Québec, Canada. The site-specific cross-validation approach is also employed, wherein models are calibrated at one study site and subsequently validated at the other site. This approach is performed to evaluate the spatial transferability of the calibrated parameters.

2. Study area and dataset

2.1. Study area

In-situ measurements of soil and vegetation characteristics were collected in two different sites (Site 1 and Site 2), all of which are located in the Province of Québec. Site 1 corresponds to Agriculture and Agri-food Canada (AAFC) experimental site at Lennoxville (45°21′52″ N, 71°48′53″ W), while Site 2 is located in the Montérégie region, near Saint Hyacinthe (45°37′52″ N, 72°57′23″ W). Data were collected in Site 1 during summers of 2022 and 2023 over soybean (*Glycine* max L.), corn (*Zea mays* L.), and wheat (*Triticum aestivum* L.) fields. Measurements in Site 2 were acquired in the summer of 2024, only over soybean fields. Fig. 1 (a) illustrates the boundaries of the soybean, wheat, and corn fields at AAFC Lennoxville. Due to crop rotation, the crop types on the same fields differ in 2022 and 2023 and are highlighted separately using colour codes (for 2022) and hatched lines (for 2023). For the Montérégie site (Fig. 1 (b)), only field locations are provided rather than the exact field boundaries due to the large distance (~10 km) between the fields. The number of agriculture fields changed from 2022 (4 soybean, 3 corn, 2 wheat) to 2023 (2 soybean, 2 corn, 4 wheat). In the Montérégie, a total of 15 soybean fields were considered in 2024.

2.2. Satellite data and preprocessing

The RADARSAT Constellation Mission (RCM), which was launched by the CSA in 2019, provides C-band (5.404 GHz) SAR data in various acquisition modes, polarizations, and spatio-temporal resolutions. The CP data that were available over our study sites are in medium

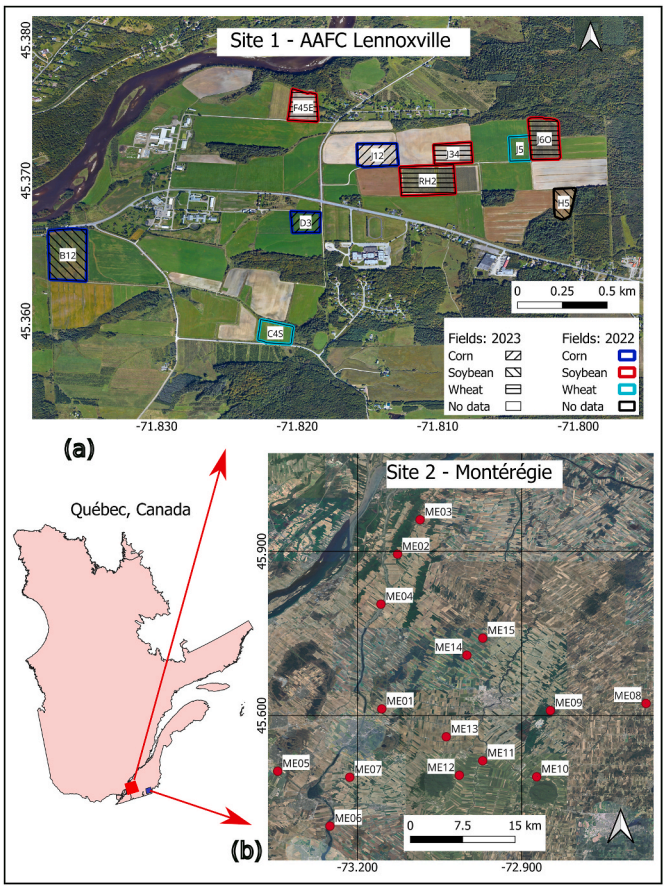

Fig. 1. (a) Field boundaries at study site 1, AAFC Lennoxville. Crop types of 2022 and 2023 are represented separately with colours (red: soybean, blue: corn, cyan: wheat) and hatched lines ('\': corn, '/': soybean, '–': wheat), (b) Locations of 15 fields at the second study site in the Montérégie region. Field boundaries are not provided, given the long distance between fields: all fields are soybean.

resolution (30 m) ScanSAR mode. The data were downloaded from the Earth Observation and Data Management System (EODMS) in the form of a 2×1 Multilooked Complex (MLC) (Canadian Space Agency, 2022a). Radiometric calibration, speckle (5×5 Boxcar) filtering, and terrain correction are done using the SNAP software (European Space Agency, 2025). TanDEM-X global digital elevation model (DEM) of 30 m spatial resolution (German Aerospace Center, 2022) is used for terrain correction and local incidence angle image generation. In ScanSAR mode, RCM acquisitions are typically performed in the 17.28° to 48.3° incidence angle range with four different sub-ranges (Canadian Space Agency, 2022b). Yet, only 20° to 43° are considered in the analysis to reduce the effect of non-circularity observed in CP data (Touzi et al., 2023). Acquisition dates and incidence angle ranges of the RCM time series are provided in Table 1. It shows that the incidence angle can vary considerably between consecutive acquisition days in our study area, with one day's measurement falling in the lower range (17.0°–28.9°), while the next day's measurement potentially falls in the upper range (33.7°–42.7°).

2.3. *In-situ* data collection and preparation

The *in-situ* soil parameters include field soil moisture (FSM), precipitation, and once-in-a-season measurements of surface roughness (root-mean-square height (*s*) and correlation length (*l*)) and texture composition. Before soil roughness measurement, the crop residues from the previous growing season were removed from the plot. The soil exhibits considerable variability in roughness with *s* and *l* values ranging from 0.8 to 2.5 cm and 6.7–12.4 cm in the Lennoxville site and 1.3–2.2 cm and 7.1–11.4 cm in the Montérégie site, respectively.

Soil texture is quite variable in its composition in terms of the percentage of sand, silt, and clay fractions, which are 17–36%, 14–55% and 14–62% in the Lennoxville site and 11–68%, 17–61%, and 17–64% in the Montérégie site. FSM measurements (m^3/m^3) from the soil surface (0–5 cm depth) were conducted with a 30 × 30 m sampling strategy to match the spatial resolution of the RCM ScanSAR data. For each crop type, the *in-situ* FSM measurements that were taken simultaneously with the RCM overpasses. The number of FSM measurements for each crop type on each acquisition day is also indicated in Table 1. Three replicate measurements were taken and averaged at each sampling point. Satellite overpasses occurred between 07:00–07:30 (Eastern Daylight Time, EDT) for the descending orbit and between 18:00–18:30 EDT for the ascending orbit over both study sites. Ground measurements were nominally conducted within a 4-h window centered on each acquisition, starting 2 h prior to the satellite overpass. In instances where logistical constraints arose, the measurement window was extended to 6 h to ensure adequate data collection. Under low to moderately wet soil conditions (FSM <0.2 m^3/m^3), the temporal offset between satellite overpass and *in-situ* measurements is not expected to introduce significant retrieval errors. However, under wetter soil conditions, this may result in uncertainties on the order of 0.02–0.05 m^3/m^3, attributable to the higher temporal variability of soil moisture (Montzka et al., 2020; Crow et al., 2012). The vegetation parameters include once-in-a-season measurements of crop density, row direction, and weekly measurements of crop height (*H*), above-ground vegetation water content (VWC), dry biomass, and crop phenology in terms of BBCH (Biologische

Table 1
Dates, orbits (Ascending (A) and Descending (D)), and incidence angle ranges of RCM acquisitions with corresponding number of *in-situ* soil moisture measurements for AAFC-Lennoxville and the Montérégie sites, for each crop type.

AAFC Lennoxville					Montérégie		
Date/Orbits	Incidence angle range (°)	No. of soil moisture measurements (sampling points)			Date/Orbits	Incidence angle range (°)	No. of soil measurements (sampling points)
		Corn	Soybean	Wheat			Soybean
2022-06-24/A	17.05–28.90	-	-	22	2024-06-28/D	33.70–42.74	33
2022-07-17/D	33.70–42.74	92	122	-	2024-07-04/D	17.05–28.90	58
2022-07-26/A	17.05–28.90	92	122	22	2024-07-14/D	17.05–28.90	52
2022-08-07/A	17.05–28.90	92	109	22	2024-07-15/D	33.70–42.74	41
2022-08-19/A	17.05–28.90	92	122	22	2024-07-16/A	17.05–28.90	69
2023-06-14/D	33.70–42.74	36	66	54	2024-07-28/D	17.05–28.90	41
2023-07-12/D	33.70–42.74	24	11	-	2024-08-07/D	33.70–42.74	38
2023-07-20/D	33.70–42.74	24	11	34	2024-08-31/D	33.70–42.74	41
2023-07-30/A	33.70–42.74	17	26	29			
2023-08-13/D	33.70–42.74	18	27	39			
2023-08-29/D	33.70–42.74	26	37	29			

Bundesanstalt, Bundessortenamt und Chemische Industrie) scale (Meier, 2018; McNairn et al., 2016). Fig. 2 (a) presents the temporal evolution of FSM, precipitation, and the RCM acquisition dates that are indicated by the black downward arrows. Fig. 2(b) and (c) and (d) present VWC (black lines) and H (red lines) for corn, wheat (both for 2022 and 2023) and soybean (all three years). An increase in measured FSM from wheat, soybean, and corn (green, orange, and purple error bars, respectively) is observed immediately following rainfall events (blue bars in Fig. 2 (a)). Across crop types, the average FSM ranged from 0.10 to 0.45 m^3/m^3.

In 2023, several saturated soil moisture conditions (FSM >0.45 m^3/m^3) attributable to frequent and heavy rain events were recorded, and the corresponding measurements were filtered out from the dataset. VWC (black) and H (red) are highly correlated during the growing season until the crop attains its peak height. However, in 2023, the VWC of wheat attains its maximum value before H, which could be due to heavy rainfall. Maximum canopy heights and water contents pairs were measured as 250 cm & 4 kg/m^2, 120 cm & 6 kg/m^2, and 100 cm & 3 kg/m^2 for corn, wheat, and soybean, respectively. Due to heavy rainfall in 2023, crop densities of corn and soybean fields were lower compared to 2022 and 2024, which explains the reduction in the VWC per unit area. To ensure the focus is exclusively on vegetated soils, only those measurements with $H > 10$ cm were included in the analysis, thereby excluding bare soil conditions.

3. Methodology

In this section, we first describe the concepts of CP, the vegetation descriptor (CpRVI), the surface scattering model (CP-AIEM), and the vegetation radiative transfer models (WCM and SSRT). We then introduce the proposed algorithms CP-AIEM-WCM and CP-AIEM-SSRT for soil moisture retrieval under crop cover.

3.1. Compact polarimetry (CP)

The SAR architecture that was designed with single polarization transmission and dual orthogonal polarization reception is known as Hybrid/Compact Polarimetry (CP) (Charbonneau et al., 2010). The most commonly used form of this architecture is the circularly (right or left) transmit linearly receive (CTLR) mode. Unlike FP SAR, there are only two channels in the CP scattering vector ($\mathbf{K}_C$) as given in (1) (Raney, 2007b): circularly transmit horizontally receive (k_{CH}) and circularly transmit vertically receive (k_{CV}).

$$\mathbf{K}_C = \begin{bmatrix} k_{CH} \\ k_{CV} \end{bmatrix} = \left(\frac{1}{\sqrt{2}}\right) \begin{bmatrix} S_{HH} & S_{HV} \\ S_{VH} & S_{VV} \end{bmatrix} \begin{bmatrix} 1 \\ \pm j \end{bmatrix} \quad \text{where, } j = \sqrt{-1} \tag{1}$$

where S_{pq} denotes the scattering matrix elements of FP SAR data, with p and q being the horizontal (H) and vertical (V) polarizations. The right and left circular polarization cases are indicated by – and + signs, respectively. CP data also be represented using the 2×2 covariance matrix ($\mathbf{C}_2$), which is the dot product of the scattering vector $\mathbf{K}_C$ and its conjugate transpose ($\mathbf{K}_C{}^{*T}$) as follows:

$$\mathbf{C}_2 = \begin{bmatrix} c_{11} & c_{12} \\ c_{21} & c_{22} \end{bmatrix} = \mathbf{K}_C \cdot \mathbf{K}_C{}^{*T} \tag{2}$$

$$\mathbf{S} = \begin{bmatrix} s_0 \\ s_1 \\ s_2 \\ s_3 \end{bmatrix} = \begin{bmatrix} C_{11} + C_{22} \\ C_{11} - C_{22} \\ C_{12} + C_{21} \\ \pm j(C_{12} - C_{21}) \end{bmatrix} = \begin{bmatrix} |k_{CH}|^2 + |k_{CV}|^2 \\ |k_{CH}|^2 - |k_{CV}|^2 \\ 2\mathrm{Re}\{k_{CH}.k_{CV}^*\} \\ \pm 2\mathrm{Im}\{k_{CH}.k_{CV}^*\} \end{bmatrix} \tag{3}$$

where C_{11}, C_{12}, C_{21}, and C_{22} are the $\mathbf{C}_2$ matrix elements, and $\mathbf{S}$ is the Stokes vector calculated from $\mathbf{C}_2$ (Cloude et al., 2012). The Stokes parameters s_0, s_1, s_2 and s_3 represent the total backscatter, dominance of

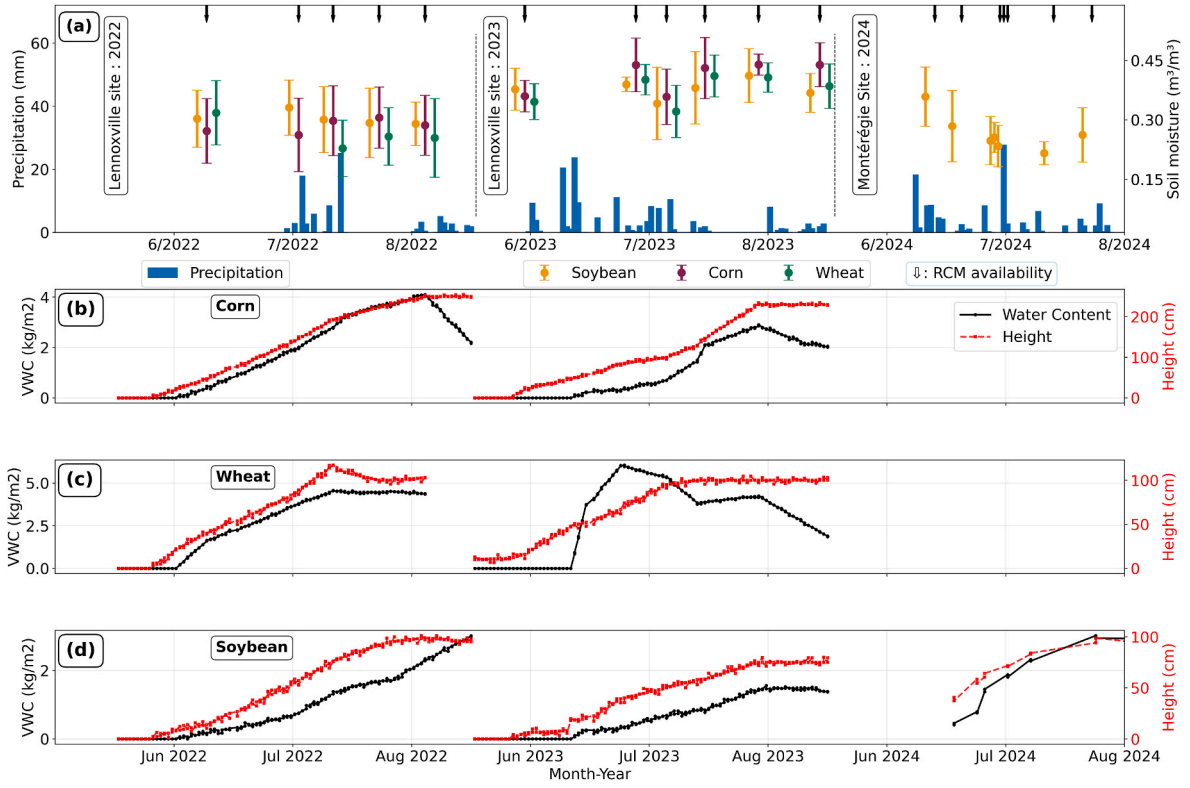

Fig. 2. (a) Temporal variation of *in-situ* precipitation (blue bars) and average FSM (error bars) for each crop type, with coding soybean in orange, corn in purple, and wheat in green for summer 2022, 2023, and 2024. For June 2022, field-level precipitation data were unavailable due to a delay in the deployment of the on-site rain gauge. FSM shows good agreement with precipitation. RCM acquisitions are also indicated by the black downward arrows at the top. Temporal evolution of VWC (black lines) and height (red lines) for (b) corn, (c) wheat, and (d) soybean. In 2024, only soybean fields were scouted in the Montérégie region, hence those blank spaces in wheat and corn plots.

the polarization component, and the real and imaginary parts of the complex cross-product, respectively (Wang et al., 2023b; Dingle Robertson et al., 2022). Different CP signatures, such as conformity, degree of polarization, and decomposition powers, are calculated from the Stokes parameters.

3.2. CP advanced Integral Equation Model (CP-AIEM)

In our previous work (Mookkuthala Erkaramana et al., 2026), we have adapted the Advanced Integral Equation Model (AIEM) (Wu and Chen, 2004; Chen et al., 2003) for the CP domain to introduce CP-AIEM by using the direct physical relationship in (1) between FP and CP scattering matrices. The field integrals (I_{CH} and I_{CV}) of CP-AIEM will thus be calculated from its FP counterparts of the AIEM (I_{HH}, I_{HV}, I_{VH} and I_{VV}) as:

$$I^n_{CH} = \frac{1}{\sqrt{2}}\left(I^n_{HH} - jI^n_{HV}\right) \tag{4}$$

$$I^n_{CV} = \frac{1}{\sqrt{2}}\left(I^n_{VH} - jI^n_{VV}\right) \tag{5}$$

CH and CV backscattering coefficients of the CP-AIEM are formulated as:

$$\sigma^0_{CH} = \frac{k_1^2}{2}\exp\left[-s^2\left(k_z^2 + k_{sz}^2\right)\right]\sum_{n=1}^{\infty}\frac{s^{2n}}{n!}|I_{CH}|^2 W^{(n)} \tag{6}$$

$$\sigma^0_{CV} = \frac{k_1^2}{2}\exp\left[-s^2\left(k_z^2 + k_{sz}^2\right)\right]\sum_{n=1}^{\infty}\frac{s^{2n}}{n!}|I_{CV}|^2 W^{(n)} \tag{7}$$

The roughness spectrum ($W^{(n)}$) of the soil surface is a function of the wavelength-scaled surface parameters *ks* and *kl* where *k* is the wave number. The terms k_z and k_{sz} are derived from the cosine of incidence and scattering angles, and k_1 denotes the spatial frequency component (Wu and Chen, 2004; Chen et al., 2003). Direct CP backscattering coefficients from the soil surface are modelled by the CP-AIEM from *in-situ* soil moisture and roughness measurements.

3.3. CP Radar Vegetation Index

The CP Radar Vegetation Index (CpRVI) (Mandal et al., 2020a) was introduced by using the concept of geodesic distance (D_{ID}), which was calculated between the Kennaugh matrix of any pixel and that of an ideal depolarizer. CpRVI is defined as the product of the damping factor (β) and the measure of similarity (f_{ID}), which are functions of D_{ID} and the Stokes parameter, as follows (Mandal et al., 2020a):

$$\text{CpRVI} = \beta f_{ID}, 0 \le \text{CpRVI} \le 1 \tag{8}$$

$$\text{where } f_{ID} = 1 - \frac{3}{2}D_{ID} \quad \text{and,} \tag{9}$$

$$\beta = \left(\frac{\min\left(\frac{s_0 - s_3}{2}, \frac{s_0 + s_3}{2}\right)}{\max\left(\frac{s_0 - s_3}{2}, \frac{s_0 + s_3}{2}\right)}\right)^{2(3/2D_{ID})} \tag{10}$$

CpRVI has been used in recent studies for crop monitoring with RCM data (Muhuri et al., 2023a; Jiao et al., 2022). In this work, we use it as an indicator of vegetation growth (status & temporal dynamics).

3.4. Water Cloud Model (WCM)

A vegetation canopy over the ground was modelled as a uniformly distributed water cloud by Attema and Ulaby (1978) under the assumption of dominance of volume scattering. The model considers the single scattering response from the cloud with a specific height and density, which are related to VWC. These considerations will allow us to formulate the total backscatter (σ^0_{Total}) from the plant-soil system as an incoherent sum of soil (σ^0_{Soil}) and canopy (σ^0_{Veg}) contributions in linear units as follows (Attema and Ulaby, 1978).

$$\sigma^0_{Total_{pq}} = A\left[1 - e^{-B\, m_w\, H \sec\theta}\right]\cos\theta + C\, e^{(D\, m_v - B\, m_w\, H \sec\theta)}\cos\theta \tag{11}$$

$$\sigma^0_{Total_{pq}} = \sigma^0_{Veg_{pq}} + \tau^2\, \sigma^0_{Soil_{pq}} \tag{12}$$

$$\sigma^0_{Total_{pq}} = AV_1\, cos\,\theta\left(1 - \tau^2\right) + \tau^2\, \sigma^0_{Soil_{pq}} \tag{13}$$

$$\tau^2 = e^{-2BV_2 \sec\theta} \tag{14}$$

In (11), θ is the local incidence angle, p and q denote the polarizations, *H* (m) is the vegetation height, and m_w (kg/m^2) and m_v (m^3/m^3) are the VWC and FSM, respectively. *A*, *B*, *C*, and *D* are empirically calibrated using multiple linear regression for each frequency. The first and second terms in (12) are respectively the vegetation and soil contributions, and the backscattering from the soil is scaled by the two-way attenuation (τ^2) of the vegetation layer (Ulaby et al., 2014). The *in-situ* parameters m_w and *H* can be replaced by remote sensing-based vegetation indicators V_1 and V_2, thereby calibrating *A* and *B* parameters accordingly (13). These indicators include Leaf Area Index (LAI) (Kumar et al., 2012), Plant Area Index (PAI) (Mandal et al., 2020b), Normalized Difference Vegetation Index (NDVI) (Inoubli et al., 2024), Normalized Difference Water Index (NDWI) (Weis et al., 2024), and the Radar Vegetation Index (RVI) (Muhuri et al., 2023b). Truncating the expression of τ^2 (14) by using the McLaurin series expansion and considering only the first two terms helps to simplify the WCM, as already applied in several previous studies (Muhuri et al., 2023b; Bai and He, 2015; Li and Wang, 2018; Mardan and Ahmadi, 2021):

$$\tau^2 = 1 - 2BV_2 \sec\theta \tag{15}$$

We adopt this simplified equation and transfer it to the CP domain. We calculate the total CP backscattering coefficients ($\sigma^0_{CH,WCM}$, $\sigma^0_{CV,WCM}$) for each polarization using the CP indices and the soil contribution that was modelled from the CP surface scattering model ($\sigma^0_{CH,CPAIEM}$, $\sigma^0_{CV,CPAIEM}$):

$$\sigma^0_{CH,WCM} = 2ABV_1V_2 + (1 - 2BV_2 \sec\theta)\,\sigma^0_{CH,CPAIEM} \tag{16}$$

$$\sigma^0_{CV,WCM} = 2ABV_1V_2 + (1 - 2BV_2 \sec\theta)\,\sigma^0_{CV,CPAIEM}$$

The vegetation contribution is represented by the term $2ABV_1V_2$. Parameters V_1 and V_2 are substituted by suitable vegetation indices to optimize for *A* and *B*. In WCM, σ^0_{Soil} can be represented in terms of an in-built empirical equation similar to (11) (Mandal et al., 2020b; Vermunt et al., 2022). Otherwise, it can be replaced by a surface backscattering model, such as the Oh model (Inoubli et al., 2024), Dubois model (Muhuri et al., 2023b) or different versions of the Integral Equation Model (Inoubli et al., 2024). In this work, we use the simulated CP-AIEM backscatters for σ^0_{Soil} and replace both V_1 and V_2 by a single parameter, i.e. CpRVI. The decision to apply CpRVI as an appropriate index has been made after multiple trials with different indices, such as the volume scattering component of different decomposition models, and NDVI that is derived from available Sentinel-2 data. The trials with CpRVI replacing both V_1 and V_2 provide the highest accuracy and lowest bias in the WCM optimization. Moreover, it is important to evaluate the potential of the model in case of the absence of *in-situ* measurements such as plant height, plant water content or cloud-free optical images. Using (16), the equations for the inverse WCM are given as follows:

$$\sigma^0_{CH,Soil} = \frac{\sigma^0_{CH,RCM} - 2ABV_1V_2}{1 - 2BV_2 \sec\theta} \tag{17}$$

$$\sigma^0_{CV,Soil} = \frac{\sigma^0_{CV,RCM} - 2ABV_1V_2}{1 - 2BV_2 \sec\theta}$$

where $\sigma^0_{CH,\ RCM}$ and $\sigma^0_{CV,\ RCM}$ denote the observed total backscattering coefficient from RCM data, while $\sigma^0_{CH,\ Soil}$ and $\sigma^0_{CV,\ Soil}$ are the direct soil backscatter estimates that are inverted from WCM for CH and CV polarizations, respectively. During WCM calibration, model parameters *A* and *B* will be optimized using the training data consisting of RCM CP backscatter and CP-AIEM backscatter that was simulated from *in-situ* FSM. During inversion, the optimized model constants will be used to calculate direct soil backscatter from independent RCM testing data to retrieve soil moisture. This approach is hereafter referred to as the CP-AIEM-WCM algorithm.

3.5. Single scattering radiative transfer (SSRT) model

The vegetation first-order single scattering radiative transfer (SSRT) model (De Roo et al., 2001) is the simplified, semi-empirical derivation of the Michigan Microwave Canopy Scattering (MIMICS) (Mcdonald et al., 1990; Tour et al., 1994), where the ground-trunk scattering response is removed due to the adaptation to soybeans (De Roo et al., 2001; Ulaby and Long, 2014). Fig. 3 illustrates the components of SSRT total backscatter, namely, direct backscatter contribution from the ground (σ^0_g), direct backscatter contribution from the canopy (σ^0_c), the combined ground-canopy and canopy-ground forward scattering contribution ($\sigma^0_{gc\ +\ cg}$), and the ground-canopy-ground scattering contribution (σ^0_{gcg}) (Weis et al., 2024; Ulaby and Long, 2014). Thus, the total SSRT backscatter can be expressed as the sum of four components at polarization p and q:

$$\sigma^0_{Total} = \sigma^0_{g_{pq}} + \sigma^0_{c_{pq}} + \sigma^0_{gc+cg_{pq}} + \sigma^0_{gcg_{pq}} \tag{18}$$

The intensities of multiple scattering components $\sigma^0_{gc\ +\ cg}$ and σ^0_{gcg} are observed to be less than −30 dB (not significant) in C-band scattering under agricultural crop conditions. Thus, they will be subsequently ignored (Zhang and Wu, 2016) and the total backscatter can be calculated by considering only the direct soil and canopy volume contributions.

$$\sigma^0_{Total} = \sigma^0_{g_{pq}} + \sigma^0_{c_{pq}} = \tau_p\tau_q\sigma^0_{soil_{pq}} + \frac{\sigma^{back}_{v_{pq}}\cos\theta}{\kappa^p_e + \kappa^q_e}\left(1 - \tau_p\tau_q\right) \tag{19}$$

The backscatter (σ^{back}_v) per unit volume of leaves (Ulaby and Long, 2014) can be expressed in two ways in terms of scattering coefficient (κ_s), depending upon the assumption of the distribution of canopy elements (Ulaby and Long, 2014):

$$\sigma^{back}_v = \begin{cases} \kappa_s, \text{Isotropic scatterers} \\ 1.5\ \kappa_s, \text{Rayleigh scatterers} \end{cases} \tag{20}$$

The extinction (κ_e) and scattering (κ_s) coefficients, and the single scattering albedo (ω), are related as follows (Ulaby and Long, 2014):

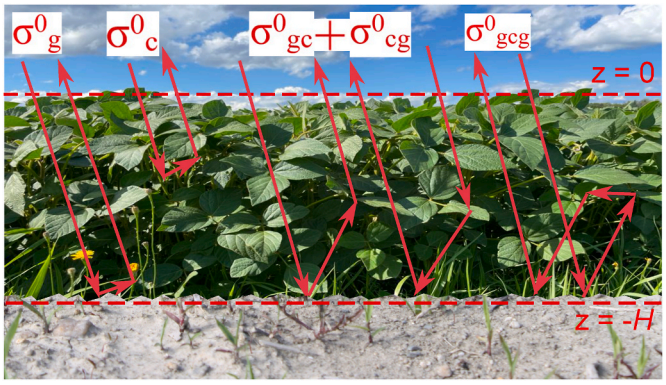

Fig. 3. Visualization of single scattering components of total backscatter in SSRT, adopted from (Ulaby and Long, 2014) undergoing interactions with the soybean plant and rough ground surface.

$$\kappa_e = a_c\sqrt{\frac{m_w}{H}} \quad \text{and} \quad \kappa_s = \omega\kappa_e \tag{21}$$

where a_c and ω are the model parameters that need to be optimized. The value of κ_e depends on the orientation, VWC (m_w) and vegetation height (H) together with the polarization of the microwaves. Vegetation optical depth and two-way attenuation (τ^2) of the vegetation for each polarization are directly proportional to κ_e (Ulaby et al., 2014). From (19), the forward and inverse SSRT equations can be defined to implement the optimization and soil moisture retrieval. In the forward model (22), $\sigma^0_g = \sigma^0_{CPAIEM,}$ which is the simulated direct soil backscatter from CP-AIEM, and $\sigma^0_{Total} = \sigma^0_{SSRT}$ is the simulated total backscatter from the SSRT.

$$\sigma^0_{SSRT} = \sigma^0_{CPAIEM} + \sigma^0_c \tag{22}$$

The term σ^0_c represents the vegetation contribution (see Eq. (19)). In the inverse model, $\sigma^0_{Total} = \sigma^0_{RCM,}$ which is the observed total backscatter from RCM CP data and $\sigma^0_g = \sigma^0_{Soil}$ is the direct soil backscatter that has been inverted by the SSRT. This implies:

$$\sigma^0_{RCM} = \sigma^0_{Soil} + \sigma^0_c \tag{23}$$

$$\sigma^0_{Soil} = \sigma^0_{RCM} - \sigma^0_c \tag{24}$$

During SSRT calibration, we optimize the model parameters a_c and ω using the training data consisting of RCM CP backscatter and CP-AIEM backscatter that is simulated from *in-situ* FSM. During inversion, the optimized model constants will be used to calculate direct soil backscatter from independent RCM testing data to retrieve soil moisture. This approach is hereafter referred to as the CP-AIEM-SSRT algorithm.

3.6. Calibration, inversion and validation of CP-AIEM-WCM and CP-AIEM-SSRT

3.6.1. Calibration

The respective calibration strategies for WCM and SSRT using the CP data and the CP-AIEM are described in Fig. 4. Backscattering from bare soil surface ($\sigma^0_{CH,\ soil}$ and $\sigma^0_{CV,\ soil}$) for CH and CV channels were modelled using CP-AIEM in (6) and (7) from *in-situ* FSM, *ks* and *kl*. From RCM data, the CH and CV backscattering coefficients ($\sigma^0_{CH,\ RCM,}$ $\sigma^0_{CV,\ RCM}$), the $\mathbf{C}_2$ matrix, Stokes vector ($\mathbf{S}$) and the incidence angle image are extracted for each FSM sampling location. We applied data segmentation to split the data into different sets of training and testing samples, while considering the observation geometry and target structure. In our study sites, the incidence angle range of RCM acquisition varies considerably from day to day. It can be 17–28° on one acquisition day and 36–43° on the next day, as summarized in Table 1. Our study suggests that CP parameters are strongly affected by θ and field conditions. It is difficult to determine whether the changes in their temporal profile are attributed to changes in θ or in the *in-situ* conditions. Moreover, the proportion of vegetation and soil contributions to the total backscatter varies with crop type and observation parameters. Considering these aspects, the RCM data were separated into two different θ-ranges ($\leq$30° and >30°), with the *in-situ* data being divided accordingly. The total number of data points per crop type is thus redistributed into two groups, yielding more insights into the behaviour of CP parameters at different stages of crop growth under similar observation conditions. In our case, we subset the training data into six categories by considering two incidence angle ranges: $\theta \leq 30°$ and $\theta > 30°$ and three crop types: corn, soybean, and wheat. Thus, the model constants in WCM and SSRT are separately optimized for each of these six cases. The threshold of 30° is selected because the RCM data in our study sites are available in a lower ($17 < \theta \leq 28°$) and a higher ($36 < \theta \leq 43°$) range of local incidence angle. Moreover, this threshold of 30° is commonly used in the literature to define the validity domain of backscattering models, making the grouping consistent with established conventions (Muhuri et al., 2023b; Dubois et al., 1995).

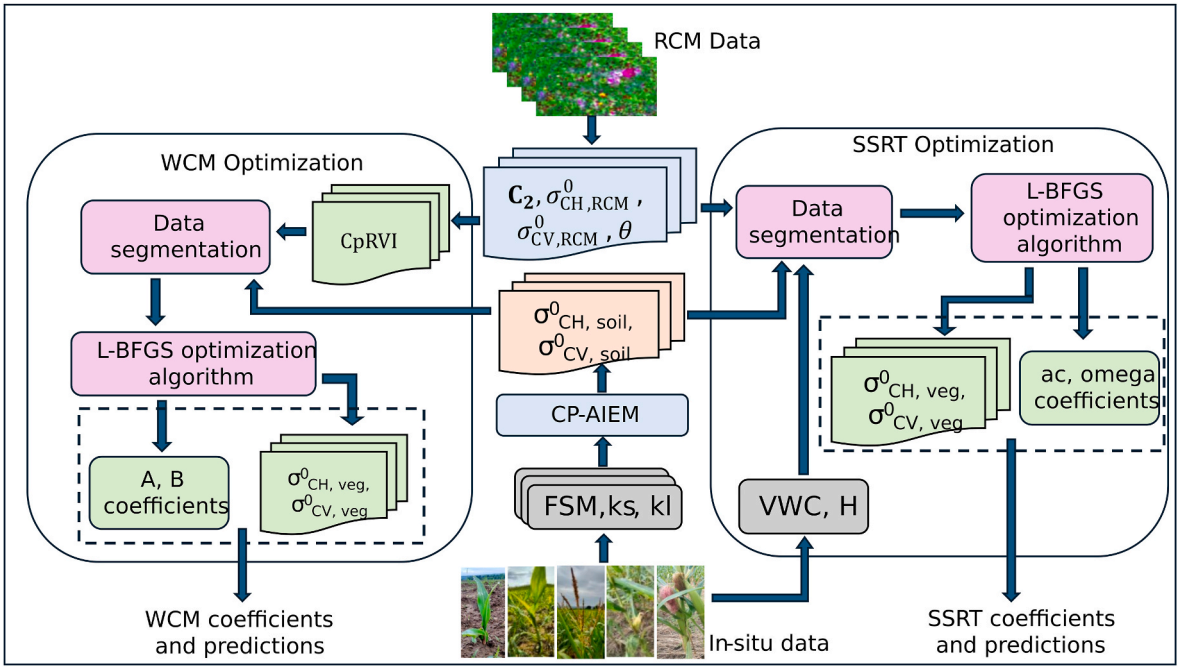

Fig. 4. Optimization strategies for the WCM and SSRT models. For the WCM model (left), CpRVI is used as the indicator of vegetation growth to calculate the vegetation scattering contribution and model coefficients. In the SSRT (right), *in-situ* VWC and *H* are directly used for optimizing the model coefficients. In both models, the soil backscatter contribution is calculated using the CP-AIEM model.

With the WCM forward model (16), the total backscattering coefficients ($\sigma^0_{CH,\ WCM}$, $\sigma^0_{CV,\ WCM}$) are calculated with inputs of the simulated vegetation contribution using CpRVI and the soil backscatter that is modelled from CP-AIEM ($\sigma^0_{CH,\ CPAIEM}$, $\sigma^0_{CV,\ CPAIEM}$), considering initial values of *A* and *B* parameters. The error between simulated and RCM backscatter is minimized using the limited memory Broyden-Fletcher-Goldfarb-Shanno algorithm (L-BFGS) (Amirabadi et al., 2023) to optimize *A* and *B*. This algorithm is well-suited for simulation-inversion optimization problems and has been widely used in previous works (Weis et al., 2024; Abassi et al., 2024). The parameters such as maximum iteration, function tolerance, and step size are chosen as 1000, 2.22×10^{-9} and 1×10^{-8} respectively, following previous implementations (Amirabadi et al., 2023). The L-BFGS loss function, L (*A, B*) is expressed as:

$$L(A,B) = \sum_i \left(\sigma^0_{CV,RCM,i} - \sigma^0_{CV,WCM,i}\right)^2 + \left(\sigma^0_{CH,RCM,i} - \sigma^0_{CH,WCM,i}\right)^2 \quad (25)$$

Where *i* iterates over the number of training samples. This algorithm requires a set of initial values and a physically realizable bound for the parameters, which are selected from previous studies and physical reasoning using the expected range of other variables (V_1, V_2, τ^2, backscattering coefficients) (Mandal et al., 2021; Weis et al., 2024). We assume that *A* and *B* are dependent on the incidence angle and crop type, but not on polarization, to simplify the optimization and to reduce the required volume of training samples.

Given that it is a semi-empirical model, SSRT requires more data to optimize the model constants (a_c and ω). From the *in-situ* VWC and *H* data, κ_e and κ_s are calculated with initial values of a_c and ω (21). As was the case for WCM, we consider a_c and ω to be dependent upon the incidence angle and crop type, but not on the polarization. The linear sum of individual terms produces $\sigma^0_{CH,\ SSRT}$, $\sigma^0_{CV,\ SSRT}$ and the error between them and $\sigma^0_{CH,\ RCM}$, $\sigma^0_{CV,\ RCM}$ is minimized to optimize a_c and ω. The L-BFGS loss function, L (a_c, ω) is expressed as:

$$L(a_c,\omega) = \sum_i \left(\sigma^0_{CV,RCM,i} - \sigma^0_{CV,SSRT,i}\right)^2 + \left(\sigma^0_{CH,RCM,i} - \sigma^0_{CH,SSRT,i}\right)^2 \quad (26)$$

Where *i* iterates over the number of training samples. Here, we have used the same set of parameters for the L-BFGS algorithm as that of CP-AIEM-WCM optimization. In this study, we have fixed the optimized parameters (*A*, *B*, a_c and ω) for a particular scenario regarding the entire phenological cycle, irrespective of crop season. While there are differences in cultivation practices and minor variations within the same crop type, we treat the entire crop type as a single case for the parameter optimization. This approach avoids the impracticality of optimizing parameters separately for each field condition, which would require extensive training data.

3.6.2. *Model inversion for soil moisture retrievals under vegetation*

The inversion of CP-AIEM-WCM and CP-AIEM-SSRT algorithms is carried out in two steps: the first step removes the scattering contribution of vegetation from the RCM CP backscattering coefficients to calculate the soil backscattering coefficient (17), (24). This involves forward modelling of vegetation volume scattering from WCM and SSRT, using the optimized values of *A*, *B* and a_c and ω, respectively, for each combination of θ-range and crop type. The vegetation contribution is subtracted from the total backscatter to calculate the soil contributions ($\sigma^0_{CH,\ Soil}$ and $\sigma^0_{CV,\ Soil}$) using (17) and (24) in the WCM and SSRT cases, respectively. In the second step, soil moisture is estimated using the CP-AIEM inversion. Since the optimization of the volume model is done separately for each combination of incidence angle range and crop type, the inversion is also performed likewise. The inversion of the dielectric constant from CP-AIEM involves a lookup table (LUT)-based two-parameter optimization (Ponnurangam et al., 2016; Merzouki et al., 2019a):

$$\Delta = \sqrt{\left(\sigma^0_{CH,Soil} - \sigma^0_{CH,LUT}\right)^2 + \left(\sigma^0_{CV,Soil} - \sigma^0_{CV,LUT}\right)^2} \quad (27)$$

where $\sigma^0_{CH,\ LUT}$ and $\sigma^0_{CV,\ LUT}$ are bare soil backscattering coefficients that are modelled from CP-AIEM using the system ranges of θ, the dielectric constant (ε), and field level values of *ks* and *kl*. Minimization of Δ is performed to select the best matching pair of $\sigma^0_{CH,\ LUT}$ and $\sigma^0_{CV,\ LUT}$ corresponding to the observed RCM backscatter. Field surface roughness

was provided as an input into the LUT-based inversion to eliminate ambiguity. Soil moisture is calculated from the dielectric constant using Dobson's model, considering the soil texture composition (Dobson et al., 1985). The performance of each inversion case (section 3.6) is then compared using Pearson correlations (r-values) with agreeable significance ($p < 0.05$) values, inversion rate (IR), root mean square error (RMSE), and the number of invertible samples (N). Here, IR signifies the ratio of N to the total number of testing samples in each case.

3.6.3. Validation strategies

The validation of the CP-AIEM-WCM and CP-AIEM-SSRT has been implemented through three train-test splitting strategies.

- The first approach combines radar observations and *in-situ* data from the Lennoxville (site 1) and Montérégie (site 2) sites, then applies stratified sampling to randomly partition the data into non-overlapping training (40%) and testing (60%) subsets. This is a well-established practice (Muhuri et al., 2023b; Zhou et al., 2025b) and ensures inclusion of all possible variability in biophysical parameters while maintaining statistical independence and unbiased validation.
- In the second approach, the models were trained using the data from the soybean fields of the Lennoxville site (4 fields in 2022 and 2 in 2023) and validated using data from the 15 soybean fields in the Montérégie site.
- In the third approach, the models were trained using the data from the 15 soybean fields of the Montérégie site and validated using the data from the soybean fields of the Lennoxville site (4 fields in 2022 and 2 in 2023).

Site-specific cross-validation strategies (the 2nd and 3rd approaches) evaluate the spatial transferability of the algorithms by training the model exclusively with the data from one study site and cross-validating at a different study site. Only soybean fields are considered because *in-situ* measurements of corn and wheat fields are not available for the Montérégie study site.

4. Results

The performance of CpRVI as a vegetation growth descriptor is first analyzed. The results of WCM and SSRT calibration are then presented. Finally, the retrieved soil moisture from the CP-AIEM-WCM and the CP-AIEM-SSRT algorithms for each inversion case and validation strategies is presented.

4.1. CpRVI as a vegetation growth indicator

Evaluation of CpRVI (orange lines) as a vegetation growth indicator is demonstrated in Fig. 5 through its temporal plots along with VWC (blue) and H (black). Each subplot represents crop type (row-wise) and incidence angle ranges $\theta \leq 30^\circ$ (left column) and $\theta > 30^\circ$ (right column) combinations. The three crop growth seasons 2022, 2023 and 2024 are indicated by the background colours (light blue, light yellow and light orange) and vertical break line. The justification for the strategy of splitting the RCM data into two incidence angle ranges ($\leq$30° and >30°) can be best described by an example of the soybean field (Fig. 5(a) and (b)). RCM observations on 2024-06-28 and 2024-07-14 (Fig. 5 (b)) were at $\theta > 30^\circ$, and the corresponding CpRVI values are 0.72 and 0.8. However, on 2024-07-04 (Fig. 5 (a)), the acquisition was at $\theta \leq 30^\circ$ and the CpRVI is 0.6. This successive decrease and increase must be due to θ-dependence of CpRVI rather than the crop conditions. The CpRVI values of 2022-07-17 (0.65, 0.75, and 0.69 for soybean, corn and wheat, respectively) are not included in the plot since it is the only acquisition of 2022 in the $\theta > 30^\circ$ range. Except for corn at $\theta > 30^\circ$, all correlations that are indicated in the plots are at the 95% confidence level. In general, CpRVI shows a similar trend and good correlation with VWC and H in all cases, except for corn at $\theta > 30^\circ$. For soybean, CpRVI has a positive correlation with H (0.71, 0.82) and VWC (0.53, 0.78) for $\theta \leq 30^\circ$ (Fig. 5

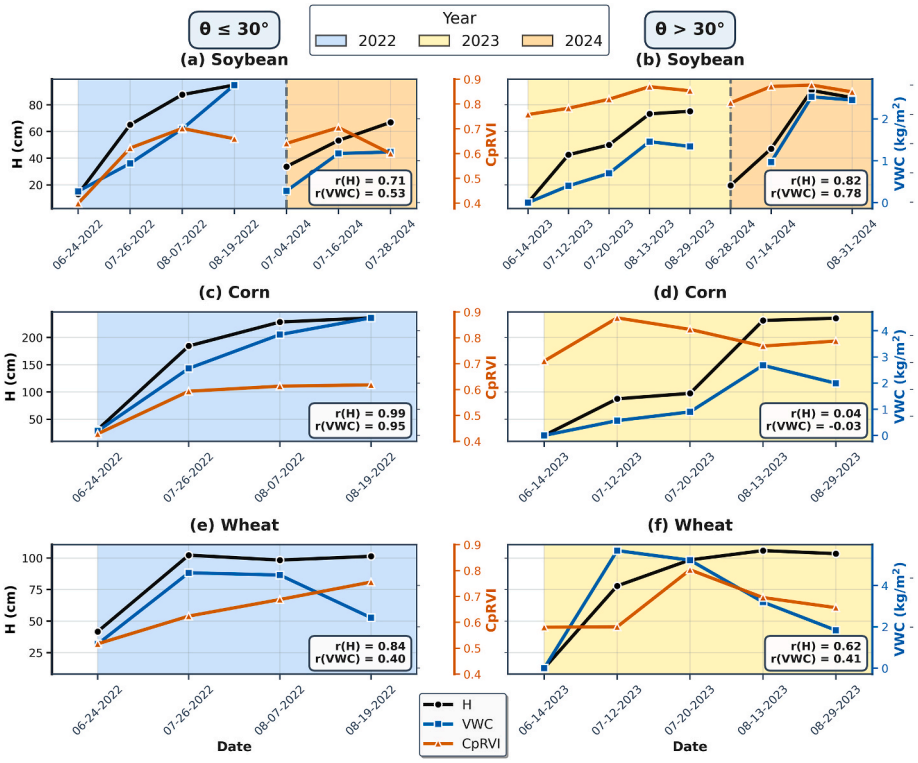

Fig. 5. Temporal variation of average CpRVI (orange) with VWC (blue) and H (black) for soybean (a, b), corn (c, d), and wheat (e, f) crops at $\theta \leq 30^\circ$ (left column) and $\theta > 30^\circ$ (right column). The growing seasons 2022, 2023 and 2024 are indicated using light blue, light yellow and light orange backgrounds. The r-values that were calculated with CpRVI versus VWC and CpRVI versus H are mentioned in each case. Except for corn at $\theta > 30^\circ$, all correlations are at the 95% confidence level.

(a)) and for $\theta > 30^\circ$ (Fig. 5 (b)), respectively. CpRVI value increases from June (0.4, 0.65) to mid-August (0.7, 0.8) and reduces towards the end of August (0.6, 0.7) at $\theta \leq 30^\circ$ and $\theta > 30^\circ$ ranges. It has slightly higher variability (0.3) at $\theta \leq 30^\circ$ as compared to $\theta > 30^\circ$ (0.15) during the soybean growth cycle. CpRVI has very high correlation (0.99 and 0.95) with H and VWC of corn at $\theta \leq 30^\circ$ (Fig. 5 (c)). However, it has a very low correlation with H (0.04, $p > 0.05$) and insignificant correlations with VWC (-0.03, $p > 0.05$) at $\theta > 30^\circ$ (Fig. 5 (d)). It varies from June to August in a narrow range of 0.45–0.65 at $\theta \leq 30^\circ$ and 0.7–0.85 at $\theta > 30^\circ$. For wheat fields, the CpRVI is correlated to VWC and H with an r value of 0.4 vs 0.84 at $\theta \leq 30^\circ$ (Fig. 5 (g)) and 0.41 vs 0.62 at $\theta > 30^\circ$ (Fig. 5 (f)). CpRVI increases from 0.5 to 0.7 at $\theta \leq 30^\circ$, while it does not reduce even though VWC declines. At $\theta > 30^\circ$, it increases from 0.6 to 0.7 and decreases back to 0.6 following VWC.

4.2. Calibration of WCM and SSRT

This section presents the results of the WCM and the vegetation SSRT calibrations. Table 2 provides the optimization accuracy of WCM and SSRT models through the minimum RMSE values between the predicted and RCM backscatter for CV and CH channels. The RMSE varies roughly between 0.7 and 2.2 dB depending on the crop type, the CP channels, and the θ ranges. In WCM, the highest RMSE (2.12 and 2.17 dB) and the lowest RMSE (1.07 and 1.06 dB) values are obtained at $\theta \leq 30^\circ$ for soybean and corn, respectively. In SSRT, the lowest RMSE was achieved at $\theta \leq 30^\circ$ for wheat (0.78 with σ^0_{CH} and 0.70 dB with σ^0_{CV}), while the highest RMSE was at $\theta > 30^\circ$ for soybean (1.59 for σ^0_{CH} and 1.99 dB for σ^0_{CV}). It is interesting to note that the cases with a smaller number of training data (corn and wheat at $\theta \leq 30^\circ$) possess less variability and low RMSE in the WCM and SSRT optimizations. Limiting the training data set of soybean to only one study site produces lower RMSE of 1.1–1.8 dB for WCM and 0.98–1.4 dB for SSRT. Thus, there is an approximate reduction of 0.4–0.7 dB as compared to the use of joined data set from both sites. Moreover, SSRT produces lower RMSE, indicating that the predictions are closer to the training samples than those of WCM.

The WCM and SSRT optimizations are verified by analyzing the two-way attenuation (τ^2) and the vegetation contribution (σ^0_{Veg}) with respect to the corresponding vegetation descriptor. Fig. 6 (a) illustrates the variation of $1 - \tau^2$ and σ^0_{Veg} in WCM with CpRVI at $\theta \leq 30^\circ$ (blue) and at $\theta > 30^\circ$ (red). As CpRVI increases, σ^0_{Veg} increases and $1 - \tau^2$ decreases in all θ-crop type cases. The dynamic range of CpRVI (x-axis) for the same crop type is different at $\theta \leq 30^\circ$ and at $\theta > 30^\circ$. Thus, the comparison is performed considering only the shared range of CpRVI in both cases. For soybean, $1 - \tau^2$ values are close at both θ-ranges, while σ^0_{Veg} is consistently higher at $\theta \leq 30^\circ$ than at $\theta > 30^\circ$. For wheat, in the same range of CpRVI, the values of $1 - \tau^2$ and σ^0_{Veg} are higher at $\theta \leq 30^\circ$ as compared to those at $\theta > 30^\circ$. For corn, for the same range of CpRVI, σ^0_{Veg} values are similar at both θ-ranges, while $1 - \tau^2$ is higher at $\theta \leq 30^\circ$ than at $\theta > 30^\circ$. The difference of σ^0_{Veg} between the two θ cases is more pronounced for wheat (~3 dB), followed by soybean (~2 dB) and corn (<1 dB).

Fig. 6 (b) illustrates the variation of $1 - \tau^2$ and σ^0_{Veg} in SSRT with respect to the vegetation indicator (VWC) at $\theta \leq 30^\circ$ (blue) and $\theta > 30^\circ$ (red). VWC has very high variability even within the same crop type, as was previously indicated in Fig. 2 (b). The variability of VWC (x-axis) for the same crop type is different at $\theta \leq 30^\circ$ and $\theta > 30^\circ$; hence, the comparison is done considering only the shared range. As VWC increases, σ^0_{Veg} increases and $1 - \tau^2$ decreases in all θ-crop type cases. For soybean, at the same range of VWC, the values of σ^0_{Veg} and $1 - \tau^2$ demonstrate the same trend at both θ-ranges. For wheat, σ^0_{Veg} and $1 - \tau^2$ are higher at $\theta \leq 30^\circ$ as compared to $\theta > 30^\circ$. For corn, there is only a minimal difference between the values of σ^0_{Veg} at the two θ-ranges, while $1 - \tau^2$ is higher at $\theta \leq 30^\circ$. The curve is better defined for WCM since only CpRVI is needed to calculate $1 - \tau^2$ while SSRT requires both VWC and H. The difference in σ^0_{Veg} between the two θ cases is more pronounced for wheat (2–4 dB), followed by soybean (1–2 dB) and corn (<1 dB).

Bar graphs in Fig. 6 (c) and (d) present the optimized parameters A and B (with hatched lines) in WCM and a_c and ω (with hatched lines) in SSRT for each θ-crop type combination. In WCM, optimized values of A for soybean are similar at both θ-ranges (0.21–0.23), and the same response is observed for corn (0.15–0.18). For wheat, A at $\theta \leq 30^\circ$ is larger than at $\theta > 30^\circ$ (0.28 vs 0.13). Parameter B for soybean at $\theta \leq 30^\circ$ is slightly larger than at $\theta > 30^\circ$ (0.25 vs 0.2). For corn, B at $\theta \leq 30^\circ$ is slightly lower than at $\theta > 30^\circ$ (0.31 vs 0.36). A larger difference of B between the cases of $\theta \leq 30^\circ$ and $\theta > 30^\circ$ (0.28 vs 0.39) is observed for wheat. The higher θ-dependence of A and B in wheat agrees with the observations in Fig. 6 (a). In SSRT, the optimized value of a_c for soybean is larger at $\theta \leq 30^\circ$ compared to $\theta > 30^\circ$ (0.40 vs 0.30). The a_c value is lower at $\theta \leq 30^\circ$ compared to $\theta > 30^\circ$ in the case of wheat (0.30 vs 0.40) and corn (0.19 vs 0.33). Parameter ω for soybean is smaller at $\theta \leq 30^\circ$ compared to that at $\theta > 30^\circ$ (0.15 vs 0.21). The value of ω is larger at $\theta \leq 30^\circ$ compared to that at $\theta > 30^\circ$ in the case of wheat (0.22 vs 0.10) and corn (0.19 vs 0.14). In SSRT, the optimized values of a_c and ω depend greatly upon θ across crop types.

Table 2
Minimum optimization RMSE (dB) values obtained for the calibration of WCM and SSRT models with RCM backscatter for each CP channel and the combinations of crop type and incidence angle.

RMSE (dB)	WCM				SSRT			
	$\theta \leq 30^\circ$		$\theta > 30^\circ$		$\theta \leq 30^\circ$		$\theta > 30^\circ$	
	σ^0_{CH}	σ^0_{CV}	σ^0_{CH}	σ^0_{CV}	σ^0_{CH}	σ^0_{CV}	σ^0_{CH}	σ^0_{CV}
Soybean	2.12	2.17	1.26	1.15	1.59	1.99	0.76	1.1
Corn	1.07	1.06	1.84	1.87	0.80	0.81	0.74	0.76
Wheat	1.35	1.14	1.73	1.81	0.78	0.70	1.08	1.22

4.3. Soil moisture inversion and validation

Soil moisture estimated from the CP-AIEM-WCM and CP-AIEM-SSRT algorithms is presented and analyzed. These results correspond to the random split validation strategy in which the combined data from the two study sites are randomly split into training (40%) and testing (60%) datasets. In Fig. 7, only the invertible pixels are shown in the scatterplots, and the inversion rate (IR) values are mentioned for each case along with other statistical measures.

The scatterplot between the estimated and predicted soil moisture from CP-AIEM-WCM is shown in Fig. 7 (a) for soybean (1 and 2), wheat (3 and 4), and corn (5 and 6) fields at $\theta \leq 30^\circ$ (left column) and at $\theta > 30^\circ$ (right column). Soil moisture estimation over soybean fields shows a moderate RMSE of 0.10 m^3/m^3 at $\theta \leq 30^\circ$ and 0.09 m^3/m^3 at $\theta > 30^\circ$. The $\theta \leq 30^\circ$ case has much higher IR (89% vs 76%) and r (0.69 vs 0.43 with p-value <0.05) compared to those at $\theta > 30^\circ$. Better soil moisture estimation accuracy during the densely vegetated stages of soybean ($H \geq 80$ cm) is achieved at $\theta \leq 30^\circ$. For wheat, the number of FSM measurements that were made was lower than for other crops. At both θ-ranges, the RMSE is the same (0.07), but the model performs better with higher r (0.76 vs 0.54 with p-value <0.05) and IR (92% vs 68%) at $\theta \leq 30^\circ$ than at $\theta > 30^\circ$. For corn, the retrieval accuracy is higher at $\theta \leq 30^\circ$ as compared to that at $\theta > 30^\circ$ with high correlation (0.81 vs 0.64 with p-value <0.05), very high IR (92% vs 17%), and lower RMSE (0.06 vs 0.07). In general, the CP-AIEM-WCM performance is better at $\theta \leq 30^\circ$ as compared to that at $\theta > 30^\circ$, regardless of crop type.

Comparison between the estimated and measured soil moisture using the CP-AIEM-SSRT algorithm is provided in Fig. 7 (b) for soybean (1 and 2), wheat (3 and 4), and corn (5 and 6) fields at $\theta \leq 30^\circ$ (left column) and at $\theta > 30^\circ$ (right column). Soil moisture that was estimated from soybean fields at $\theta \leq 30^\circ$ and at $\theta > 30^\circ$ shows similar performance in terms of IR (83% vs 86%) and RMSE (0.09, 0.08), with a difference in r (0.55 vs 0.69 with p-value <0.05). However, at $\theta > 30^\circ$, most of the inverted samples correspond to medium vegetation height ($40 < H \leq 80$ cm). Most of the samples with higher vegetation height ($H \geq 200$ cm) are inverted at $\theta \leq 30^\circ$. For wheat fields, there is higher IR (77% vs 49%) and r (0.30 vs

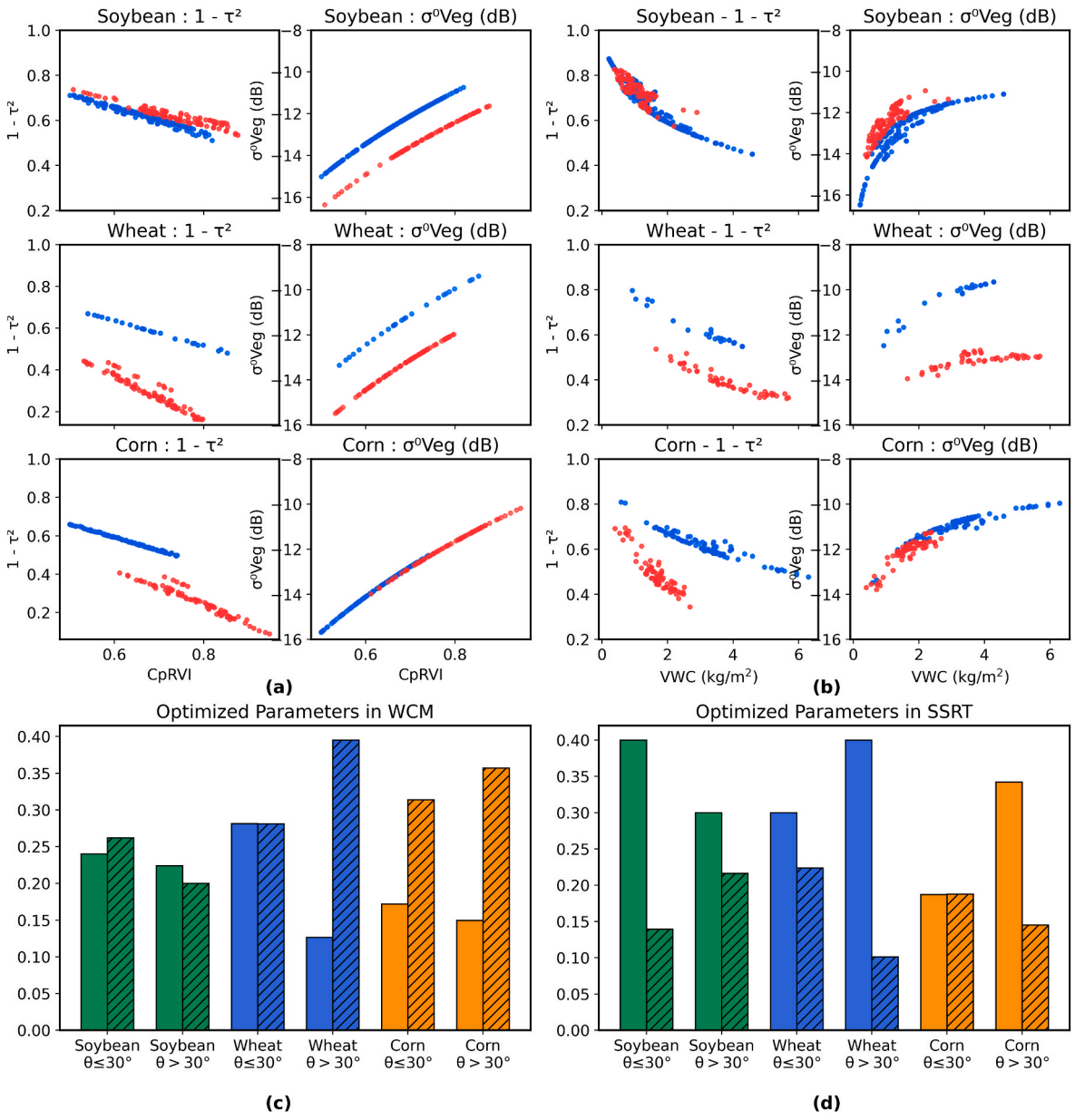

Fig. 6. Calibration of WCM (left panels) and SSRT (right panels) (a) variation of modelled two-way attenuation in terms of 1 - τ^2 and vegetation contribution (σ^0_{Veg}) vs CpRVI in WCM at $\theta \leq 30^\circ$ (blue) and $\theta > 30^\circ$ (red), (b) variation in modelled 1 - τ^2 and σ^0_{Veg} vs VWC in SSRT at $\theta \leq 30^\circ$ (blue) and $\theta > 30^\circ$ (red) (c) optimized A and B (with hatched lines) for WCM, and (d) optimized parameters a_c and ω (with hatched lines) for SSRT. Plots (c) and (d) are generated for each combination of crop type (green: soybean, blue: wheat, orange: corn) and θ-range.

0.16) but similar RMSE (0.07 vs 0.08) at $\theta \leq 30^\circ$ as compared to those at $\theta > 30^\circ$. In both cases, the p-values (0.13 and 0.31) are not significant at the 95% level. Under densely vegetated conditions ($H > 50$ cm), the model performs better at $\theta \leq 30^\circ$, similar to the trend that was observed in soybean. For corn fields, soil moisture is estimated with higher accuracy at $\theta \leq 30^\circ$, having higher IR (92% vs 43%), lower RMSE (0.08 vs 0.09), and lower r-values (0.59 vs 0.81 with p-value <0.05) compared to those at $\theta > 30^\circ$. Very high IR of 92% is achieved for corn fields at $\theta \leq 30^\circ$ (both models) and for wheat fields at $\theta \leq 30^\circ$ (CP-AIEM-WCM). Similarly, high IR values of 83–89% are achieved for soybean fields at $\theta \leq 30^\circ$ (from both models) and at $\theta \leq 30^\circ$ (from CP-AIEM-SSRT). The statistical metrics that were considered show that, in all cases except high incidence observations ($\theta > 30^\circ$) of corn fields, CP-AIEM-WCM exhibits more accurate estimates of soil moisture as compared to CP-AIEM-SSRT. Under fully grown crop canopy conditions, $\theta \leq 30^\circ$ observations show better accuracy than those under $\theta > 30^\circ$.

4.4. Temporal evolution of estimated soil moisture and comparison between CP-AIEM-WCM and CP-AIEM-SSRT algorithms

For each crop type, the temporal variation of the average values (only invertible pixels) of the estimated soil moisture from CP-AIEM-WCM and CP-AIEM-SSRT algorithms is compared with the measured field soil moisture (FSM) (Fig. 8). These results correspond to the random split validation strategy in which the combined data from the two study sites is randomly split into training (40%) and testing (60%) datasets. These averages include the variability within a field as well as that among the other fields of the same crop type. The uncertainty of each retrieval is indicated by the error bars in representing one standard deviation. The average soil moisture fluctuates roughly between 0.10 and 0.45 m^3/m^3 with peak values occurring in July and August 2023 due to several rain events (Fig. 2 (a)). Soil moisture retrievals from both models generally follow the same pattern of FSM.

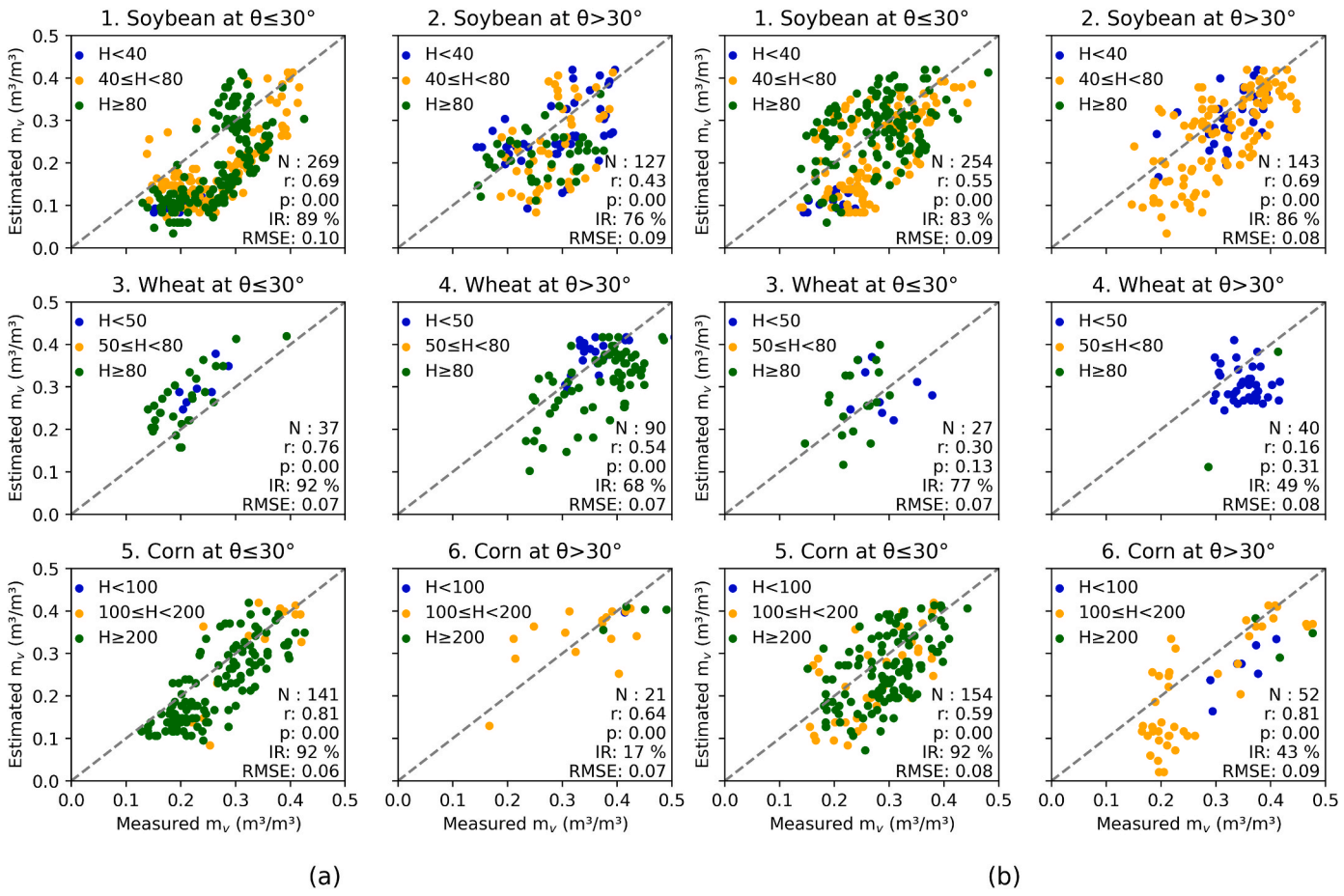

Fig. 7. Statistical comparison of soil moisture retrieval for (a) CP-AIEM-WCM and (b) CP-AIEM-SSRT algorithms by crop type and incidence angle (θ) range combinations. For each crop type, the points are colour-coded according to the different ranges of vegetation heights (H). Random splitting of training (40%) and testing (60%) is performed on the combined dataset from both study sites. Only invertible pixels are shown in the plots.

The variability that is visualized in the FSM is fairly replicated in both model predictions, as indicated by the error bars, except in a few cases. For example, for soybean (Fig. 8 (a)), there is greater variability for estimated soil moisture from the CP-AIEM-SSRT (date: 2023-06-14) compared to FSM. Similarly, the estimated soil moisture from the CP-AIEM-WCM on 2023-07-20 has lower variability than FSM. In terms of overall RMSE, CP-AIEM-SSRT outperforms CP-AIEM-WCM for soybean (0.04 vs 0.06 m^3/m^3). In contrast, CP-AIEM-SSRT has a lower accuracy for corn (0.08 vs 0.04 m^3/m^3) and wheat (0.10 vs 0.07 m^3/m^3) as compared to CP-AIEM-WCM. For soybean (Fig. 8 (a)), CP-AIEM-SSRT performs better in 2022 (0.02 vs 0.06 m^3/m^3) and 2024 (0.06 vs 0.08 m^3/m^3) compared to CP-AIEM-WCM, where the soil was moderately wet (FSM = 0.15–0.3 m^3/m^3). Both models have comparable RMSEs (0.03 m^3/m^3) in 2023, a year that was characterized by heavy rainfall and higher soil moisture (0.35–0.45 m^3/m^3) conditions. In corn fields (Fig. 8 (b)), CP-AIEM-WCM has lower RMSEs of 0.03 vs 0.07 m^3/m^3 under dry soil conditions (2022) when compared to CP-AIEM-SSRT. It also outperforms CP-AIEM-SSRT under wet soil conditions (2023) as well (0.04 vs 0.08 m^3/m^3). Compared to CP-AIEM-SSRT, CP-AIEM-WCM exhibits a lower RMSE in wheat fields for wet soil conditions (0.07 vs 0.13 m^3/m^3) but higher RMSE in dry soil (0.06 vs 0.03 m^3/m^3), as seen in Fig. 8 (c)).

It should be noted that in 2022, the estimates are well-aligned with the measurements because the RCM observations were at $\theta \leq 30°$. In 2023, where the soil was consistently wet throughout the season, CP-AIEM-SSRT underestimates soil moisture relative to CP-AIEM-WCM for all crops.

4.5. Transferability of the developed algorithms between sites

We have performed three validation strategies to evaluate the transferability of the calibrated models: (1) combine data from both sites and perform random train-test splitting, (2) train the models using the data from site 1 and validate with site 2 data, (3) train the models using the data from site 2 and validate with site 1 data. Since *in-situ* measurements for wheat and corn are not available from site 2 (Montérégie), we analyze the transferability of the approach only for soybean crops. The scatterplots and temporal variation of estimated soil moisture are not presented for the site-specific cross-validation approaches. Yet, the accuracy is shown in Table 3 in terms of statistics corresponding to each θ range for both CP-AIEM-WCM and CP-AIEM-SSRT algorithms.

CP-AIEM-WCM performance is consistent in terms of RMSE in the three train-test splitting strategies, with 0.10 m^3/m^3 for $\theta \leq 30°$ and 0.09 m^3/m^3 for $\theta > 30°$, and in terms of r-values with 0.66–0.69 for $\theta \leq 30°$ and 0.43–0.47 for $\theta > 30°$. When the training and testing samples are from different study sites, degradation is observed in the number of invertible pixels and their corresponding IR values. The highest IR value is obtained with random splitting of the complete dataset (89% and 76%), compared to using an external testing site. IR decreases when the model is trained with data from site 1 and tested at site 2 (78% and 45%), or when the sources of the training and testing datasets are reversed (71% and 65%) for $\theta \leq 30°$ and for $\theta > 30°$, respectively. CP-AIEM-SSRT follows a similar trend, with comparable RMSE for $\theta > 30°$ (0.08–0.09) and for $\theta \leq 30°$ (0.09–0.10) among the different train-test splitting strategies. In terms of r, the random split strategy (0.55 and 0.69) performs better than training with data from

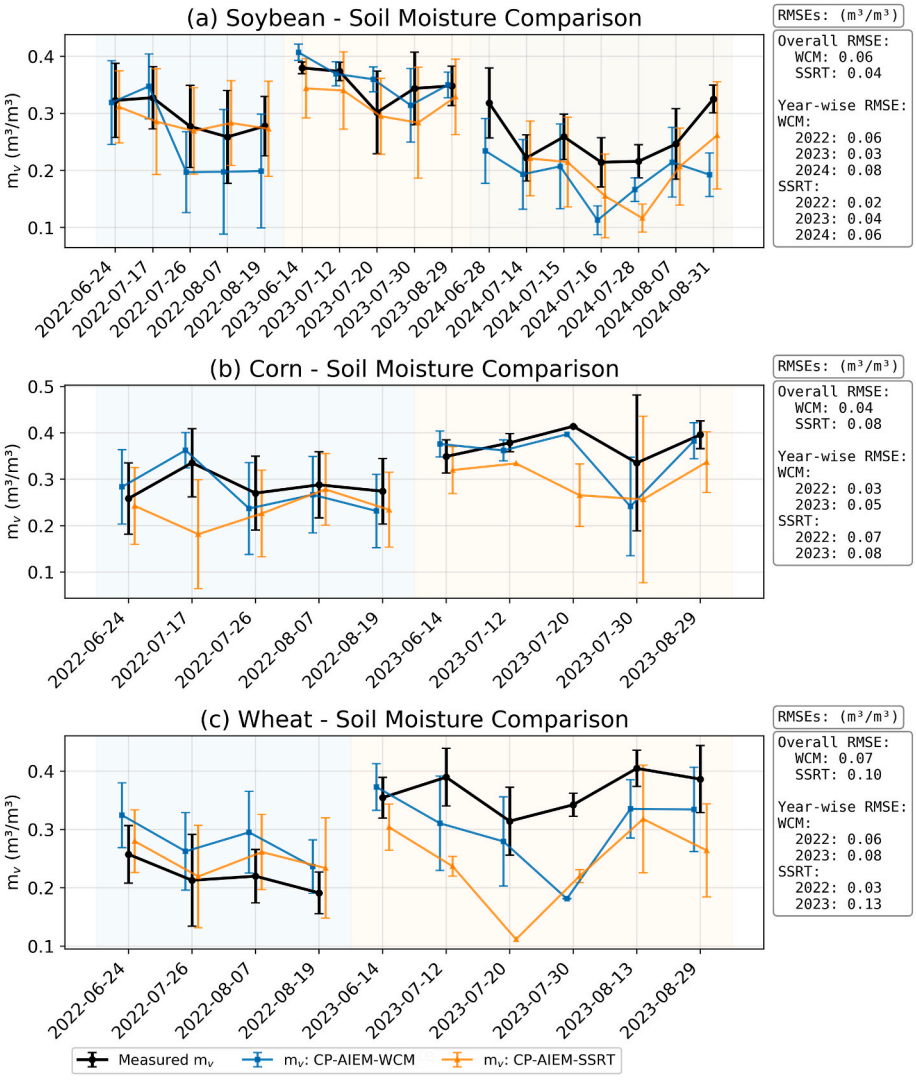

Fig. 8. Temporal variation of measured (black lines) and estimated soil moisture that was averaged for each crop from both algorithms for (a) soybean, (b) corn, and (c) wheat. Soil moisture estimated from the CP-AIEM-WCM and the CP-AIEM-SSRT algorithms is represented by blue and orange lines, respectively. Error bars represent the variability of soil moisture within crop type. Overall and year-wise RMSEs of both algorithms are also indicated in each subplot. The validation strategy is the random train-test splitting.

Table 3
Comparison between training-testing strategies for soybean fields. Site 1: AAFC Lennoxville and Site 2: Montérégie. All r-values are significant at the 95% confidence level.

Model	Splitting strategy	$\theta \leq 30^\circ$				$\theta > 30^\circ$			
		No. of Train: Test samples	RMSE	IR (%)	r	No. of Train: Test samples	RMSE	IR (%)	r
CP-AIEM-WCM	Random train- test split (40:60)	229:344	0.10	89	0.69	181: 272	0.09	76	0.43
	Site 1: Training Site 2: Testing	353:220	0.10	78	0.67	153: 300	0.09	45	0.46
	Site 2: Training Site 1: Testing	220:353	0.10	71	0.66	300: 153	0.09	65	0.47
CP-AIEM-SSRT	Random train-test split (40:60)	229:344	0.09	83	0.55	181: 272	0.08	86	0.69
	Site 1: Training Site 2: Testing	220:353	0.10	76	0.49	153: 300	0.09	75	0.58
	Site 2: Training Site 1: Testing	353:220	0.09	67	0.48	300: 153	0.08	66	0.61

site 1 and testing on site 2 (0.49 and 0.58) or vice versa (0.48 and 0.61) for $\theta \leq 30^\circ$ and for $\theta > 30^\circ$, respectively. Slight degradation in IR is observed from the random splitting (83% and 86%) to the first (76% and 75%) and second (67% and 66%) study site-specific cross-validation strategies for $\theta \leq 30^\circ$ and for $\theta > 30^\circ$, respectively. Thus, the cross-validation accuracies are sufficiently encouraging even though there is degradation of ~10% in IR compared to random train-test splitting.

5. Discussion

This study provides insight into the adaptation and calibration of radiative transfer models for C-band CP SAR observations over agriculture fields to retrieve surface soil moisture. The developed algorithms, which were denoted as CP-AIEM-WCM and CP-AIEM-SSRT, are empirically calibrated with RCM CP backscatters and *in-situ* soil and vegetation measurements. CP-AIEM was introduced in our previous study (Mookkuthala Erkaramana et al., 2026) where we demonstrated its higher potential for retrieving soil moisture under bare rough soil surface conditions as compared to empirical and machine learning methods.

5.1. Performance of CP Radar Vegetation Index (CpRVI)

Various vegetation descriptors, such as NDVI, entropy, Radar Vegetation Index (RVI), and Generalized Radar Vegetation Index (GRVI), among others, have been previously investigated to replace V_1 and V_2 in WCM for FP SAR-based soil moisture estimation (Muhuri et al., 2023b). Volume scattering components of CP decomposition models (m-χ and m-δ) have also been previously considered for this purpose (Mandal et al., 2021). The analysis from our experimental sites reveals that CpRVI exhibits higher correlation with H (0.71–0.99) and VWC (0.40–0.95) when compared to many other descriptors (in every θ-crop type combination except corn at $\theta > 30°$). For example, entropy and volume scattering components of m-χ decomposition showed non-significant correlations with H (p-value >0.05), and moderate correlations with VWC (ranging from 0.50 to 0.70). Therefore, CpRVI was adopted in this study because it displayed the highest correlations with H and VWC among other potential CP SAR vegetation descriptors.

CpRVI exhibits a higher dynamic range for $\theta \leq 30°$ compared to $\theta > 30°$. This is because the C-band signal better interacts with the underlying crop structure at $\theta \leq 30°$ (Bindlish and Barros, 2001). For $\theta > 30°$, the signal interacts mainly with the upper canopy layers, and CpRVI saturates even at the early stages of crop growth. In all θ-crop type cases, CpRVI increases during the initial stages of crop growth until the maximum plant height is attained. It further decreases during the maturation stage for soybean at both θ-ranges and wheat at $\theta > 30°$. This decrease is attributed to the reduction in VWC as crops undergo senescence, which is also observed in FP RVI at C-band (Kim et al., 2014). The non-significant decrease in CpRVI during maturation of wheat at $\theta \leq 30°$ (Fig. 5 (e)) has previously reported in (Mandal et al., 2020a) for some crop varieties. The performance of CpRVI for soybean and wheat fields at $\theta \leq 30°$ is consistent with the previous study (Mandal et al., 2020a) except minor differences, potentially due to the crop varieties, planting and environmental conditions. For corn fields, the low dynamic range of CpRVI (under both θ-ranges) suggests the dominance of volume scattering response from the upper layer of the canopy throughout the crop cycle (El et al., 2019). The occurrence of the peak of CpRVI during the vegetative stage of corn growth (Fig. 5 (d), Date: 2023-07-12) at $\theta > 30°$ and its subsequent reduction remains unclear and requires further investigation. However, it can be due to the development of vertical structures which offer significant double bounce scattering in addition to volume scattering. Neither the performance of CpRVI for corn, nor at $\theta > 30°$, has been encountered in the literature that would permit a comparison with our findings. This analysis highlights the potential of CpRVI as an indicator of vegetation growth in the WCM optimization, rather than directly using *in-situ* H and VWC values, recognizing its limited performance at $\theta > 30°$.

5.2. Calibration of radiative transfer models

5.2.1. Simplification of WCM and its implications

WCM has the simplest radiative transfer architecture with only surface and volume scattering terms. The soil backscattering contribution term of WCM is replaced by the simulated backscatter from CP-AIEM rather than using the standard model equation (Attema and Ulaby, 1978; Mandal et al., 2020b, 2021), the Dubois model (Muhuri et al., 2023b) or IEM (Lievens and Verhoest, 2011). The use of CP-AIEM and McLaurin series simplification of WCM facilitates straightforward estimation of model parameters (A and B). We use this simplification following the lead of several previous studies, recognizing the fact that truncation assumes low vegetation conditions (Muhuri et al., 2023b; Bai and He, 2015; Li and Wang, 2018; Mardan and Ahmadi, 2021). This truncation suppresses the non-linearity of WCM and underestimates the actual attenuation through vegetation. This led to an overestimation of the soil contribution under dense vegetation conditions, resulting in lower IR values. A very small number of inverted data points for $\theta > 30°$ are attributed to this effect, when $H > 100$ cm for corn. For dense corn fields, soil moisture may be overestimated by 0.04–0.10 m^3/m^3 when $H > 100$ cm, based on our simulation analysis. Moreover, the parameters optimized including the training data with high VWC (>2 kg/m^2) may not transfer reliably to early-season or sparse vegetation conditions, regardless of crop type. According to the simulation analysis performed for soybean and wheat, there can be overestimation of soil moisture as large as 0.06 m^3/m^3 when $H > 50$ cm. However, our results obtained from CP data do not clearly demonstrate the overestimation of soil moisture in soybean and wheat. The optimization process may have partially compensated for transmissivity approximation errors by adjusting A and B values to incorporate high biomass cases. This could explain why the retrieved parameters show reasonable statistical performance. However, we adopt this method as a practical trade-off between computational efficiency and model performance. Correlation of CpRVI with VWC and H is essential for utilizing it as the vegetation descriptor in WCM.

5.2.2. Assumptions in SSRT and their implications

In contrast to WCM, SSRT is a first-order model and contains the multiple scattering terms in the total backscatter. In this study, the values of $\sigma^0_{gc\text{-}cg}$ (<-30 dB) and σ^0_{gcg} (<-40 dB) simulated using the SSRT forward model show that they are not significant in the C-band under agriculture crop conditions. Similar results are reported for higher-order scattering in (Zhang and Wu, 2016). Therefore, we excluded multiple scattering terms from the forward and inverse models. We used *in-situ* VWC and H in the process of SSRT optimization. Indeed, both VWC/H and H are separately required to invert the model. Using *in-situ* values is a constraint and a limitation, given that they are not always available. For instance, *in-situ* measurements were not available for VWC >3 kg/m^2 in the soybean and corn fields for $\theta > 30°$. This situation may introduce biases to the model optimization. Further work would be necessary in forthcoming research to determine suitable and accurate proxies for various ranges of both VWC and H. This would strengthen optimization and favour the practical use of the model. Moreover, the assumption made in this study regarding constant scattering albedo (ω) during the phenological cycle might have contributed to errors in the results. Nevertheless, we have recognized the dependence of ω on crop type and θ and have separately optimized for each θ-crop type case. The dependence of CP-AIEM-SSRT on in-situ measurements of VWC and H for both calibration and inversion severely constrains its practical applicability, making it less suitable for large-scale or real-time monitoring than the CP-AIEM-WCM. This suggests the requirement of investigating potential proxies for VWC, H, and surface roughness, using CP or other remote sensing observations to facilitate the inversion and practical use of the CP-AIEM-SSRT approach. Integrating multi-sensor remote sensing proxies, such as optical vegetation indices for VWC estimation and SAR interferometry or LiDAR for height retrieval, could substantially reduce the reliance on in-situ measurements. However, it is necessary to quantify the error propagation in the proxy-based approaches. Current work has highlighted the potential for applying these models to different sites for which they were not calibrated.

We assume that the WCM and SSRT coefficients A, B, a_c, and ω are independent of polarization to maintain simplicity of optimization.

These are uniquely calculated for both circular-linear (CH and CV) polarization channels, unlike separate calculations that have been proposed by different studies. These coefficients represent first order vegetation properties (structure and attenuation) that may exhibit similar behavior across polarizations, particularly in randomly oriented canopies. Previous studies have successfully applied polarization-independent WCM formulations for agricultural crops during certain growth stages (Mandal et al., 2020b; Inoubli et al., 2024; Muhuri et al., 2023b). The high correlation between $\sigma^0_{CH,\ RCM}$ and $\sigma^0_{CV,\ RCM}$ during low crop growth conditions suggests that the polarization independence of *A, B,* a_c, and ω could be a reasonable assumption. We could not observe any major difference in optimization RMSE (0.02–0.07 dB) between the polarization-independent optimization and polarization-specific optimization. Under dense vegetation cover (for all crop types), separate optimization of coefficients for CV and CH polarizations resulted in 0.1–0.5 dB lower RMSE compared to the polarization-independent formulation. This demonstrates that the channel-specific parameterization improves retrieval performance when canopy attenuation is significant. However, we maintain a trade-off between the simplicity and accuracy of optimization by assuming the model coefficients are independent of polarization. Moreover, we have analyzed the values of optimal parameters for each combination of crop type and incidence angle of SAR observations. The optimization RMSE for soybean is higher than that for wheat and corn over both θ ranges. The potential reasons could be the larger size of the training dataset for soybean and the associated sources of errors, including higher variability of incidence angle, crop varieties and soil moisture conditions. The positive relationship between the vegetation indicator (CpRVI or VWC) with modelled two-way attenuation (τ^2 or the inverse relationship with $1 - \tau^2$) and vegetation contribution (σ^0_{Veg}) underscores the physical significance of the WCM and SSRT optimizations. The higher value of $1 - \tau^2$ and lower vegetation contribution for $\theta \leq 30^\circ$ compared to $\theta > 30^\circ$ in the C-band validates our assertion that the optimal parameter values are physically meaningful. Fig. 6 (a) and (b) confirm that θ and crop type affect the absolute value of $1 - \tau^2$ and σ^0_{Veg} but not the fundamental trend (Mandal et al., 2021).

Most of the RCM observations in 2022 were at $\theta \leq 30^\circ$, wherein the VWC from soybean fields ranges from 1 to 4.5 kg/m^2 and that from corn fields ranges from 1 to 6 kg/m^2. In 2023, the observations were at $\theta > 30^\circ$, while the VWC of soybean ranges from 1 to 2.5 kg/m^2, and that of corn ranges from 1 to 3 kg/m^2. This significant difference in the VWC between different seasons brings variability in the training data and enhances the applicability of optimization. The analysis of the optimal parameters indicates that they are sensitive to θ-crop type combinations, and the SSRT parameters (a_c and ω) are more sensitive to θ than the WCM parameters (*A* and *B*). This is because in WCM, the effect of θ on the backscattering coefficient is compensated, in part, by the θ-dependency of CpRVI. In SSRT, the vegetation descriptors are VWC and *H*, which are crop biophysical variables that are independent of θ. *A, B,* a_c, and ω are also considered to be invariant during the complete phenological cycle (all seasons) for a particular θ-crop type combination. This assumption is appropriate because the vegetation descriptor (CpRVI or VWC) that is used in the WCM and SSRT already contains information on vegetation growth. However, these constants (*A, B,* a_c, and ω) do not appear to be universal and are hardly generalizable.

5.3. Soil moisture retrieval and validation

This section first discusses the soil moisture estimation using the random training-testing split strategy illustrated in Figs. 7 and 8. The developed CP-AIEM-WCM and CP-AIEM-SSRT approaches work consistently across crop types and θ-ranges by providing soil moisture retrievals with RMSE from 0.06 to 0.10 m^3/m^3, correlation (r) from 0.45 to 0.81 and inversion rate (IR) from 17 to 92%. Except for corn at $\theta > 30^\circ$ (IR = 17%), all cases have very high IR values (68–92%). The difference in the number of data points in the scatterplots (Fig. 7) is because only the invertible pixels are presented together with the IR values. In general, CP-AIEM-WCM and CP-AIEM-SSRT perform better (in terms of r, IR) at $\theta \leq 30^\circ$ as compared to $\theta > 30^\circ$ for all three crops. The RMSE values are comparable across all θ-ranges; consequently, the discussion focuses on the observed differences in r and IR.

In Fig. 7 (a), CP-AIEM-WCM has higher r and IR for soybean at $\theta \leq 30^\circ$, due to the greater dynamic range of CpRVI with crop growth relative to $\theta > 30^\circ$. For $\theta > 30^\circ$, the number of inverted pixels (*N*) was less during the vegetative stage ($40 \leq H < 80$) because CpRVI is saturated (0.8–0.9) at this range (Fig. 5 (b)). This causes bias in the optimization and results in deterioration of IR. At $\theta \leq 30^\circ$, and when $H \geq 80$, soil moisture is underestimated because of the very high CpRVI values. Moreover, WCM has shown its potential for soybean because the water droplet assumption is reasonable for its canopy (Zhang and Wu, 2016). CP-AIEM-WCM has higher r and IR for wheat at $\theta \leq 30^\circ$, even though both θ-ranges have a similar dynamic range of CpRVI and optimization accuracy. This could be the result of the higher two-way attenuation offered by the wheat canopy to the C-band signal at $\theta > 30^\circ$, as shown in Fig. 6 (a) and in (El et al., 2019). CP-AIEM-WCM has higher r and IR for corn at $\theta \leq 30^\circ$, due to higher dynamic range and the higher correlation of CpRVI with *H* and VWC when compared to $\theta > 30^\circ$. The significant change in IR between $\theta \leq 30^\circ$ and $\theta > 30^\circ$, especially for $H \geq 200$ cm, which highlights the influence of θ on the penetration capability of the C-band signal. There were only few measurements taken for corn when $H < 100$ cm, and all of them were $\theta > 30^\circ$. Due to the very high CpRVI in this case (Fig. 5 (d)), CP-AIEM-WCM overestimates σ^0_{Veg} and underestimates soil moisture.

In Fig. 7 (b), CP-AIEM-SSRT performs slightly better (r, IR) for $\theta > 30^\circ$ for soybean, where its canopy scattering clearly dominates over surface scattering (Zhang and Wu, 2016). This is attributed to the representation of the volume scattering term by the *in-situ H* and VWC. Its performance is not surprising because SSRT takes into account absorption and scattering for the fully grown crops. For $\theta \leq 30^\circ$, there is a greater possibility of multiple scattering, which is neglected in the modelling process. This is confirmed by the lower IR that was observed at the fully grown stages ($H > 80$). For wheat, CP-AIEM-SSRT has insignificant r-values ($p > 0.05$) in both θ-ranges, pointing to the limited applicability of SSRT to this crop. It can also be due to the smaller number of *in-situ H* and VWC measurements during this period to calibrate the model. CP-AIEM-SSRT has lower r and IR for corn at $\theta > 30^\circ$, because of saturation of backscattering coefficients, especially when $H \geq 200$ cm (El et al., 2019). This saturation is due to the lower penetration capability of the C-band signal for $\theta > 30^\circ$.

In summary, CP-AIEM-WCM and CP-AIEM-SSRT exhibit complementary strengths across different evaluation scenarios because of their respective model architectures, input parameters and optimization accuracies. The original SSRT (De Roo et al., 2001) uses the Oh model as the surface scattering model, while we utilize the theoretical model, CP-AIEM, to have a wider validity range. The Oh-SSRT was applied to FP SAR data for $\theta > 30^\circ$ and has a better RMSE of 0.02 m^3/m^3 from soybean fields with $m_v < 0.25$ m^3/m^3 (De Roo et al., 2001). At the same time, CP-AIEM-SSRT provide 0.04 m^3/m^3, considering the same range of m_v and θ (special case of Fig. 7(b)). This can be because the Oh model is calibrated specifically for less wet conditions when compared to our fields (Oh et al., 1992). The simplified vegetated soil interaction model that was proposed in (Roy et al., 2024) has lower RMSE (0.05–0.06 m^3/m^3) in C-band FP at $\theta > 30^\circ$ for wheat when compared to our CP-AIEM-WCM and CP-AIEM-SSRT. This can be because of the unavailability of a separate cross-pol channel in CP, which has a higher correlation with vegetation growth (Rotzer et al., 2017). Our algorithms provide greater accuracy at $\theta > 30^\circ$ for corn (0.07 vs 0.09 m^3/m^3) and wheat (0.07 vs 0.09 m^3/m^3) as compared to the vegetation compensation using CP m-α_s decomposition utilized in (Ponnurangam et al., 2016). This advocates the use of calibrated radiative transfer models instead of the CP decomposition. The time series change detection method of RCM data (Zhou et al., 2025a; Zhou and Wang, 2023)

performs better than our algorithms in terms of RMSE estimation for soybean (0.09 vs 0.03–0.07 m^3/m^3) and corn (0.07 vs 0.03–0.06 m^3/m^3) for $\theta > 30^\circ$ fields. Yet, time-series methods lack the deeper understanding of the scattering mechanisms and are likely to be more data and site-dependent (Cheng et al., 2023).

The temporal comparison (Fig. 8) of both algorithms demonstrates that the variability of estimated soil moisture from CP-AIEM-WCM slightly better follows the variability in FSM than does CP-AIEM-SSRT, regardless of crop type. CP-AIEM-WCM performs better than the CP-AIEM-SSRT algorithm in terms of overall RMSE for corn (0.04 vs 0.08 m^3/m^3) and wheat (0.07 vs 0.10 m^3/m^3) fields. For soybean fields, CP-AIEM-SSRT has comparatively lower RMSE (0.04 vs 0.06 m^3/m^3) than CP-AIEM-WCM. The better performance of SSRT in soil moisture estimation under soybean as compared to corn or wheat is not surprising because it is explicitly constructed for soybean, where ground-trunk scattering is insignificant (De Roo et al., 2001). In the case of wheat, the lack of sufficient training samples as compared to other crops is certainly a limiting factor in the developed and tested approach. Both models have good accuracy (RMSE of 0.02–0.06 m^3/m^3) under dry soil conditions as compared to wet soil. There is an underestimation of soil moisture (10–20%) in both models during very wet conditions (0.4–0.45 m^3/m^3), regardless of crop type. One of the possible reasons can be the parametrization of surface roughness in the CP-AIEM, given that its value can be altered by heavy precipitation (Verhoest et al., 2008). Indeed, intense rainfall events can modify the micro-topography of the soil surface through processes such as crust formation, erosion, or compaction, leading to deviations from the assumed roughness conditions in the model. As a result, the backscatter response may be misrepresented, introducing uncertainties in the retrieved soil moisture values. Moreover, the saturation of the radar signal to very wet soil conditions, reduces its sensitivity to further increases in soil moisture (Sato et al., 2025). This limitation prevents accurate estimation of soil moisture, which is particularly critical under conditions close to saturation. CP-AIEM-SSRT significantly underestimates soil moisture for wheat fields on 2023-07-20, which is due to the smaller number of *in-situ* training samples for this condition ($\theta > 30^\circ$, wet soil and high VWC). This anomaly is not observed in CP-AIEM-WCM, since it does not require *in-situ* VWC. Ultimately, there could be limitations in soil moisture retrieval using C-band due to its lower penetration through dense vegetation, due to the assumptions adopted in WCM and SSRT. Under moderate and highly vegetated conditions, the multiple scattering can be important if the soil is wet (El et al., 2019; Joseph et al., 2010). However, in this study, we have not considered the effects of multiple scattering in C-band.

Three validation strategies were performed in this work: (1) random training-testing split, (2) model training on site 1 and testing on site 2, and (3) model training on site 2 and testing on site 1 (Table 3). The main difference between the soybean fields of both sites are the crop height and density (Fig. 2). Soybean plants in Lennoxville were shorter and denser while those in Montérégie were taller but less dense. Moreover, there are considerable difference in the surface roughness and texture compositions as previously indicated in Section 2.3. The random-split strategy performs better in terms of all statistical measures because the training and testing data are independent but share the same field and environmental conditions. For $\theta \leq 30^\circ$, when the models are trained using site 1 and tested on site 2, a reduction in IR is reported due to the differences in field conditions. However, r and RMSE are still comparable because the training dataset size is larger than the testing dataset in this case. When the model is trained on the site 2 dataset having a smaller and less wet conditions (Fig. 2), the absence of extreme soil moisture conditions introduces high bias. This causes the model to underfit the true variability of the target variable. Consequently, when tested on the larger site 1 dataset which captures a fuller range of soil moisture conditions (Fig. 2), the model is expected to generalize poorly and produces systematic prediction errors. This has resulted in a larger reduction in IR and r when compared to the random split. For $\theta > 30^\circ$, the reduction in IR and r in both models is more severe, due to the stronger influence of crop characteristics on backscatter. Overall, there is consistency in RMSE across all three validation strategies (random-split, training from site-1 and testing on site-2 and vice versa), together with a reduction in the correlation and IR during cross-validation. Between the two algorithms, CP-AIEM-WCM demonstrates slightly better stability and lower deterioration during cross-validation when compared to CP-AIEM-SSRT. One possible reason could be the dependence of SSRT on the *in-situ* parameters (H and VWC), which can vary (10–15%) between test sites. In the case of WCM, CpRVI is a normalized and bounded index, unlike *in-situ* parameters, and therefore, CP-AIEM-WCM is more stable across different study sites. Although passive microwave downscaling approaches have shown good potential for large-scale soil moisture mapping (Meng et al., 2024), the SAR-based retrieval employed here offers a distinct advantage by directly providing field-scale resolution without the additional uncertainty introduced by multi-step spatial disaggregation procedures.

The algorithms demonstrate robust performance under sparse-to-moderate vegetation cover coupled with $\theta \leq 30^\circ$. Conversely, retrieval accuracy degrades under dense canopy conditions combined with $\theta > 30^\circ$, where vegetation attenuation limits soil signal penetration. While the current dataset does not permit precise quantitative thresholds for dielectric constant, incidence angle and surface roughness, these results suggest that steeper viewing geometries should be prioritized in high-biomass agricultural regions. Future work should systematically characterize the validity domain through controlled experiments across defined vegetation density and incidence angle gradients to establish quantitative performance boundaries.

6. Conclusions and future perspectives

The development of algorithms based on radiative transfer models for compensating the effect of agriculture vegetation cover on compact polarimetric radar signals to retrieve soil moisture under vegetation is the focus of this research study. The main contributions of this research are the two soil moisture retrieval algorithms: CP-AIEM-WCM and CP-AIEM-SSRT. These were developed by calibrating the WCM and the vegetation SSRT models for CP backscatter. Incidence angle and crop type are key variables that drive the values of calibrated empirical parameters (A and B). Direct volume scattering response of crop canopy is represented by CpRVI in CP-AIEM-WCM, while *in-situ* vegetation water content and height are used for CP-AIEM-SSRT. Between the two approaches, CP-AIEM-WCM performs slightly better than CP-AIEM-SSRT in terms of statistical metrics (RMSE, r and IR). Best soil moisture inversion results are obtained for corn, followed by soybean and wheat crops, using both models for $\theta \leq 30^\circ$. Three training-testing strategies are applied, including the random split approach and two site-specific cross-validations. The results indicate that models that are trained on one site can potentially be used on a different site, demonstrating their transferability. Based on the observed performance trends, we propose a preliminary validity domain for the approaches.

A key limitation of this work is the requirement for *in-situ* measurements of soil and vegetation, particularly for CP-AIEM-SSRT algorithm optimization. Overall, CpRVI appears to be a good proxy for replacing *in situ* vegetation parameters in the application of the CP-AIEM-WCM model. The current SSRT implementation requires in-situ VWC and H measurements, limiting operational scalability. Future studies should explore remote sensing proxies for VWC, H, and surface roughness using compact polarimetry or complementary observations, incorporating sources such as optical vegetation indices and SAR interferometry or LiDAR. We must quantify the error propagation in proxy-based approaches to fully realize the practical potential of the algorithms demonstrated here. The transferability assessment was performed exclusively for soybean fields due to the availability of data from both study sites (AAFC Lennoxville and Montérégie). For corn and wheat fields, since there was no validation data available from Site 2, no cross-

validation experiment was conducted. While the results suggest promising spatial transferability of the algorithm, this conclusion is presently limited to soybean crops across geographically proximate study sites sharing similar climatic conditions and crop types. Therefore, the applicable scope of spatial transferability should be understood within these constraints, specifically for the same crop type and climatic zone, and should not be broadly generalized without further validation. Application of the algorithm to more heterogeneous environments (different climatic zones, diverse crop types, and varying soil characteristics) as well as its intercomparison with other SAR and passive microwave methods, remains to be addressed in future studies. Comprehensive validation efforts, incorporating large-scale datasets spanning a wide range of soil types, crop varieties, and environmental conditions and ultimately extending to multi-frequency analysis will be essential to fully characterize model accuracy and delineate its limitations.

CRediT authorship contribution statement

Bhanu Prakash Mookkuthala Erkaramana: Conceptualization, Data curation, Formal analysis, Investigation, Methodology, Software, Validation, Visualization, Writing – original draft, Writing – review & editing. **Kalifa Goïta:** Conceptualization, Data curation, Formal analysis, Funding acquisition, Investigation, Methodology, Project administration, Resources, Supervision, Writing – review & editing. **Ramata Magagi:** Conceptualization, Data curation, Formal analysis, Funding acquisition, Investigation, Methodology, Project administration, Resources, Supervision, Writing – review & editing. **Anke Fluhrer:** Conceptualization, Data curation, Formal analysis, Investigation, Methodology, Software, Writing – review & editing. **Florian Hellwig:** Data curation, Formal analysis, Methodology, Software, Writing – review & editing. **Tanya Copley:** Data curation, Formal analysis, Funding acquisition, Project administration, Resources, Writing – review & editing. **Thomas Jagdhuber:** Conceptualization, Data curation, Formal analysis, Investigation, Methodology, Supervision, Writing – review & editing.

Declaration of competing interest

The authors declare that they have no known competing financial interests or personal relationships that could have appeared to influence the work reported in this paper.

Acknowledgement

This study was funded by the Canadian Space Agency Class Grant and the Contribution Program (21SUESAMMI) as part of the Canadian plan for spatial missions of soil moisture, together with the Natural Science and Engineering Research Council of Canada (NSERC: RPGIN, RGPIN-2017-05533, RGPIN-2024-05199, CREATE 543360-2020), and Fonds de Recherche du Québec – Nature et Technologie (FRQNT: Programme de recherche en partenariat - Agriculture durable 355658). We thank Agriculture and Agri-Food Canada (Sherbrooke) and the participating farmers for site access, students and technicians of the University of Sherbrooke, and Centre de recherche sur les grains (CÉROM), Québec, for their help with *in-situ* data collection. We thank Mitacs for the Globalink Research Award (FR129155) that supported international collaboration and enabled a multi-month research stay with the University of Augsburg's Institute of Geography. We thank William F.J. Parsons for editing the English text.

Data availability

Data will be made available on request.

References

Abassi, M., Ezzahar, J., Kheddioui, E.M., Boujoudi, B., 2024. Assessment of the effects of winter wheat scattering on SAR backscatter for soil moisture estimation based on a radiative transfer model. Eur J Remote Sens 57. https://doi.org/10.1080/22797254.2024.2394780.

Amirabadi, M.A., Kahaei, M.H., Nezamalhosseini, S.A., 2023. Active learning for OPM in FMF systems. Phys. Commun. 58. https://doi.org/10.1016/j.phycom.2023.102042.

Attema, E.P.W., Ulaby, F.T., 1978. Vegetation modeled as a water cloud. Radio Sci. 13, 357–364. https://doi.org/10.1029/RS013i002p00357.

Bai, X., He, B., 2015. Potential of Dubois model for soil moisture retrieval in prairie areas using SAR and optical data. Int. J. Rem. Sens. 36, 5737–5753. https://doi.org/10.1080/01431161.2015.1103920.

Balenzano, A., Mattia, F., Satalino, G., Davidson, M.W.J., 2011. Dense temporal series of C- and L-band SAR data for soil moisture retrieval over agricultural crops. IEEE J. Sel. Top. Appl. Earth Obs. Remote Sens. 4, 439–450. https://doi.org/10.1109/JSTARS.2010.2052916.

Bindlish, R., Barros, A.P., 2001. Parameterization of vegetation backscatter in radar-based, soil moisture estimation. Remote Sens. Environ. 76, 130–137.

Brisco, B., Li, K., Tedford, B., Charbonneau, F., Yun, S., Murnaghan, K., 2013. Compact polarimetry assessment for rice and wetland mapping. Int. J. Rem. Sens. 34, 1949–1964. https://doi.org/10.1080/01431161.2012.730156.

Canada Centre for Remote Sensing, 2005. Advanced radar polarimetry tutorial. WwwCcrsNrcanGcCa 1–97. http://www.ccrs.nrcan.gc.ca/resource/tutor/polarim/pdf/polarim_e.pdf. (Accessed 11 September 2019).

Canadian Space Agency, 2022a. RCM Multi-Look Complex (MLC) Product Type RCM Multi-Look Complex (MLC) Product Type-Additional Information.

Canadian Space Agency, 2022b. RCM Compact-Pol Calibration Status Update RCM Compact-Pol Calibration Status.

Charbonneau, F.J., Brisco, B., Raney, R.K., McNairn, H., Liu, C., Vachon, P.W., et al., 2010. Compact polarimetry overview and applications assessment. Can. J. Rem. Sens. 36, S298–S310.

Chauhan, N.S., 1997. Soil moisture estimation under a vegetation cover: combined active passive microwave remote sensing approach. Int. J. Rem. Sens. 18, 1079–1097. https://doi.org/10.1080/014311697218584.

Chen, K.S., Wu, T.D., Tsang, L., Li, Q., Shi, J., Fung, A.K., 2003. Emission of rough surfaces calculated by the integral equation method with comparison to three-dimensional moment method simulations. IEEE Trans. Geosci. Rem. Sens. 41, 90–101. https://doi.org/10.1109/TGRS.2002.807587.

Cheng, G., Huang, Y., Li, X., Lyu, S., Xu, Z., Zhao, Q., et al., 2023. Change detection methods for remote sensing in the last decade: a comprehensive review. Journal of Latex Class Files.

Chirakkal, S., Haldar, D., Misra, A., 2017. Evaluation of hybrid polarimetric decomposition techniques for winter crop discrimination. Prog. Electromagn. Res. M 55, 73–84. https://doi.org/10.2528/PIERM17011603.

Cloude, S.R., Goodenough, D.G., Chen, H., 2012. Compact decomposition theory. IEEE Geosci. Remote Sens. Lett. 9, 28–32. https://doi.org/10.1109/LGRS.2011.2158983.

Crow, W.T., Berg, A.A., Cosh, M.H., Loew, A., Mohanty, B.P., Panciera, R., et al., 2012. Upscaling sparse ground-based soil moisture observations for the validation of coarse-resolution satellite soil moisture products. Rev. Geophys. 50. https://doi.org/10.1029/2011RG000372.

Dabboor, M., Xu, J., Vakalopoulou, M., Bélair, S., Powers, J., Carrera, M., et al., 2024. The RADARSAT constellation mission for soil moisture retrieval of bare soil by compact polarimetry and random forest regression. Can. J. Rem. Sens. 50. https://doi.org/10.1080/07038992.2024.2356688.

De Roo, R.D., Du, Y., Ulaby, F.T., Dobson, M.C., 2001. A semi-empirical backscattering model at L-Band and C-Band for a soybean canopy with soil moisture inversion. IEEE Trans. Geosci. Rem. Sens. 39.

Di, Martino G., Di Simone, A., Iodice, A., 2024. Polarimetric Two-Scale Model for Soil Moisture Estimation from Hybrid Compact Polarimetry SAR Data. Institute of Electrical and Electronics Engineers (IEEE), pp. 4457–4460. https://doi.org/10.1109/igarss53475.2024.10642885.

Dingle Robertson, L., McNairn, H., Jiao, X., McNairn, C., Ihuoma, S.O., 2022. Monitoring crops using compact polarimetry and the RADARSAT constellation mission. Can. J. Rem. Sens. 1–21. https://doi.org/10.1080/07038992.2022.2121271.

Dobson, M.C., Ulaby, F.T., Hallikainen, M.T., El-Rayes, M.A., 1985. Microwave dielectric behavior of wet soil-part II: dielectric mixing models. IEEE Trans. Geosci. Rem. Sens. GE-23, 35–46. https://doi.org/10.1109/TGRS.1985.289498.

Dubois, P., van Zyl, J., Engman, T., 1995. Corrections to "measuring soil moisture with imaging radars. IEEE Trans. Geosci. Rem. Sens. 33, 1340–1340.

El, Hajj M., Baghdadi, N., Bazzi, H., Zribi, M., 2019. Penetration analysis of SAR signals in the C and L bands for wheat, maize, and grasslands. Remote Sens (Basel) 11. https://doi.org/10.3390/rs11010031.

European Space Agency, 2025. Sentinel Application Platform.

German Aerospace Center, 2022. The TanDEM-X 30m Edited Digital Elevation Model (EDEM) and DEM Change Maps (DCM).

Inoubli, R., Constantino-Recillas, D.E., Monsiváis-Huertero, A., Farah, L.B., Farah, I.R., 2024. Assessment of surface scattering models within the water cloud model toward soil moisture retrievals using Sentinel-1 and Sentinel-2 images. IEEE J. Sel. Top. Appl. Earth Obs. Remote Sens. 17, 17412–17429. https://doi.org/10.1109/JSTARS.2024.3462591.

Jackson, T.J., Schmugge, J., Engman, E.T., 1996. Remote sensing applications to hydrology: soil moisture. Hydrol. Sci. J. 41, 517–530. https://doi.org/10.1080/02626669609491523.

Jiao, X., McNairn, H., Yekkehkhany, B., Dingle Robertson, L., Ihuoma, S., 2022. Integrating Sentinel-1 SAR and Sentinel-2 optical imagery with a crop structure

dynamics model to track crop condition. Int. J. Rem. Sens. 43, 6509–6537. https://doi.org/10.1080/01431161.2022.2142077.
Joseph, A.T., van der Velde, R., O'Neill, P.E., Lang, R., Gish, T., 2010. Effects of corn on C- and L-band radar backscatter: a correction method for soil moisture retrieval. Remote Sens. Environ. 114, 2417–2430. https://doi.org/10.1016/j.rse.2010.05.017.
Joseph, A.T., Van Der Velde, R., O'Neill, P.E., Lang, R.H., Gish, T., 2008. Soil moisture retrieval during a corn growth cycle using L-band (1.6 GHz) radar observations. IEEE Trans. Geosci. Rem. Sens. 46, 2365–2374. https://doi.org/10.1109/TGRS.2008.917214.
Kim, Y., Jackson, T., Bindlish, R., Hong, S., Jung, G., Lee, K., 2014. Retrieval of wheat growth parameters with radar vegetation indices. IEEE Geosci. Remote Sens. Lett. 11, 808–812. https://doi.org/10.1109/LGRS.2013.2279255.
Kim, Y., Van Zyl, J.J., 2009. A time-series approach to estimate soil moisture using polarimetric radar data. IEEE Trans. Geosci. Rem. Sens. 47, 2519–2527. https://doi.org/10.1109/TGRS.2009.2014944.
Kornelsen, K.C., Coulibaly, P., 2013. Advances in soil moisture retrieval from synthetic aperture radar and hydrological applications. J. Hydrol. (Amst.) 476, 460–489. https://doi.org/10.1016/j.jhydrol.2012.10.044.
Kumar, K., Hari Prasad, K.S., Arora, M.K., 2012. Estimation of water cloud model vegetation parameters using a genetic algorithm. Hydrol. Sci. J. 57, 776–789. https://doi.org/10.1080/02626667.2012.678583.
Lavalle, M., 2009. Full and Compact Polarimetric Radar Interferometry for Vegetation Remote Sensing. University of Rennes.
Li, J., Wang, S., 2018. Using SAR-derived vegetation descriptors in a water cloud model to improve soil moisture retrieval. Remote Sens (Basel) 10. https://doi.org/10.3390/rs10091370.
Liang, P., Moghaddam, M., Pierce, L., 2004. Backscattering simulation for nonuniform forest canopies using multi-layer MIMICS. IEEE Geoscience and Remote Sensing Symposium.
Lievens, H., Verhoest, N.E.C., 2011. On the retrieval of soil moisture in wheat fields from L-band SAR based on water cloud modeling, the IEM, and effective roughness parameters. IEEE Geosci. Remote Sens. Lett. 8, 740–744. https://doi.org/10.1109/LGRS.2011.2106109.
Liu, B., Hao, X., Chen, Y., 2022. Backscattering characteristics of forest canopy for radio fuze. In: EEI 2022; 4th International Conference on Electronic Engineering and Informatics.
Liu, C an, Chen, Z xin, Shao, Y., Chen, J song, Hasi, T., Pan, H zhu, 2019. Research advances of SAR remote sensing for agriculture applications: a review. J. Integr. Agric. 18, 506–525. https://doi.org/10.1016/S2095-3119(18)62016-7.
Mandal, D., Bhattacharya, A., Rao, Y.S., 2021. Remote Sensing for Crop Biophysical Parameter Estimation. Springer Remote Sensing/Photogrammetry.
Mandal, D., Kumar, V., Lopez-Sanchez, J.M., Bhattacharya, A., McNairn, H., Rao, Y.S., 2020b. Crop biophysical parameter retrieval from Sentinel-1 SAR data with a multi-target inversion of water cloud model. Int. J. Rem. Sens. 41, 5503–5524. https://doi.org/10.1080/01431161.2020.1734261.
Mandal, D., Ratha, D., Bhattacharya, A., Kumar, V., McNairn, H., Rao, Y.S., et al., 2020a. A Radar vegetation index for crop monitoring using compact polarimetric sar data. IEEE Trans. Geosci. Rem. Sens. 58, 6321–6335. https://doi.org/10.1109/TGRS.2020.2976661.
Mardan, M., Ahmadi, S., 2021. Soil moisture retrieval over agricultural fields through integration of synthetic aperture radar and optical images. GIsci Remote Sens 58, 1276–1299. https://doi.org/10.1080/15481603.2021.1974276.
Mcdonald, K.C., Dobson, M.C., Ulaby, F.T., 1990. Using MIMICS to model L-Band multitemporal backscatter walnut orchard multiangle and from a. IEEE Trans. Geosci. Rem. Sens. 28.
McNairn, H., Jackson, T.J., Powers, J., Bélair, S., Berg, A., Bullock, P., et al., 2016. SMAP Validation Experiment 2016 in Manitoba, Canada-Experimental Plan.
McNairn, H., Merzouki, A., Pacheco, A., Fitzmaurice, J., 2012. Monitoring soil moisture to support risk reduction for the agriculture sector using RADARSAT-2. IEEE J. Sel. Top. Appl. Earth Obs. Remote Sens. 5, 824–834. https://doi.org/10.1109/JSTARS.2012.2192416.
Meier, U., 2018. Growth Stages of mono- and Dicotyle -donous Plants: BBCH Monograph. Germany. Federal Biological Research Centre for Agriculture and Forestry. https://doi.org/10.5073/20180906-074619.
Meng, X., Zeng, J., Yang, Y., Zhao, W., Ma, H., Letu, H., et al., 2024. High-resolution soil moisture mapping through passive microwave remote sensing downscaling. Innov. Geosci. 2. https://doi.org/10.59717/j.xinn-geo.2024.100105.
Merzouki, A., McNairn, H., Powers, J., Friesen, M., 2019a. Synthetic aperture radar (SAR) compact polarimetry for soil moisture retrieval. Remote Sens (Basel) 11. https://doi.org/10.3390/rs11192227.
Merzouki, A., McNairn, H., Powers, J., Friesen, M., 2019b. Synthetic aperture radar (SAR) compact polarimetry for soil moisture retrieval. Remote Sens (Basel) 11. https://doi.org/10.3390/rs11192227.
Montzka, C., Cosh, M., Bayat, B., Al Bitar, A., Berg, A., Bindlish, R., et al., 2020. Soil Moisture Product Validation Good Practices Protocol. https://doi.org/10.5067/doc/ceoswgcv/lpv/sm.001.
Mookkuthala Erkaramana, B.P., Jagdhuber, T., Goïta, K., Magagi, R., Fluhrer, A., Hellwig, F., et al., 2026. Development and comparison of bare soil moisture retrieval methods for compact polarimetric data. IEEE Trans. Geosci. Rem. Sens. https://doi.org/10.1109/TGRS.2026.3666196.
Moreira, A., Prats-Iraola, P., Younis, M., Krieger, G., Hajnsek, I., Papathanassiou, K.P., 2013. A tutorial on synthetic aperture radar. IEEE Geosci. Remote Sens. Mag. 1, 6–43. https://doi.org/10.1109/MGRS.2013.2248301.
Muhuri, A., Goita, K., Magagi, R., Wang, H., 2023b. Soil moisture retrieval during crop growth cycle using satellite SAR time-series. IEEE J. Sel. Top. Appl. Earth Obs. Remote Sens. https://doi.org/10.1109/JSTARS.2023.3280181.
Muhuri, A., Goïta, K., Magagi, R., Wang, H., 2023a. Geodesic distance based scattering power decomposition for compact polarimetric SAR data. IEEE Trans. Geosci. Rem. Sens. https://doi.org/10.1109/TGRS.2023.3304710, 1–1.
Oh, Y., Sarabandi, K., Ulaby, F.T., 1992. An empirical model and an inversion technique for radar scattering from bare soil surfaces. IEEE Trans. Geosci. Rem. Sens. 30, 370–981.
Ponnurangam, G.G., Jagdhuber, T., Hajnsek, I., Rao, Y.S., 2016. Soil moisture estimation using hybrid polarimetric SAR data of RISAT-1. IEEE Trans. Geosci. Rem. Sens. 54, 2033–2049. https://doi.org/10.1109/TGRS.2015.2494860.
Raney, R.K., 2006. Hybrid-polarity SAR architecture. International Geoscience and Remote Sensing Symposium (IGARSS) 3846–3848. https://doi.org/10.1109/IGARSS.2006.986.
Raney, R.K., 2019. Hybrid dual-polarization synthetic aperture radar. Remote Sens (Basel) 11. https://doi.org/10.3390/rs11131521.
Raney, R.K., 2021. Polarimetric portraits. Earth Space Sci. 8. https://doi.org/10.1029/2021EA001768.
Raney, R.K., Cahill, J.T.S., Patterson Wesley, G., Bussey, D.B.J., 2012. The m-chi decomposition of hybrid dual-polarimetric radar data with application to lunar craters. J. Geophys. Res. Planets 117. https://doi.org/10.1029/2011JE003986.
Raney, R.K., 2007a. Hybrid-polarity SAR architecture. IEEE Trans. Geosci. Rem. Sens. 45, 3397–3404. https://doi.org/10.1109/TGRS.2007.895883.
Raney, R.K., 2007b. Hybrid-polarity SAR architecture. IEEE Trans. Geosci. Rem. Sens. 45, 3397–3404. https://doi.org/10.1109/TGRS.2007.895883.
Rotzer, K., Montzka, C., Entekhabi, D., Konings, A.G., McColl, K.A., Piles, M., et al., 2017. Relationship between vegetation microwave optical depth and cross-polarized backscatter from multiyear aquarius observations. IEEE J. Sel. Top. Appl. Earth Obs. Remote Sens. 10, 4493–4503. https://doi.org/10.1109/JSTARS.2017.2716638.
Roy, S., Prasad, R., Singh, S.K., Srivastava, P.K., Singh, G., Srivastava, H.S., et al., 2024. Integration of modified water cloud and dubois models with novel interaction terms for precise estimation of soil moisture and leaf area index from C-band SAR data (preprint). https://ssrn.com/abstract=4963946. https://doi.org/10.2139/ssrn.4963946.
Sato, N., Aoki, S., Kobayashi, D., Maruo, Y., Kodaira, S., Noborio, K., 2025. Improving soil moisture estimation in wet soils using L-band synthetic aperture radar (SAR) through polarization and filtering optimization. Sci. Remote Sens. 12. https://doi.org/10.1016/j.srs.2025.100290.
Schmugge, T.J., 1983. Remote Sensing of Soil Moisture: Recent Advances, vol. 1. Addison-Wesley Publishing Company.
Steele-Dunne, S.C., McNairn, H., Monsivais-Huertero, A., Judge, J., Liu, P.W., Papathanassiou, K., 2017. Radar remote sensing of agricultural canopies: a review. IEEE J. Sel. Top. Appl. Earth Obs. Remote Sens. 10, 2249–2273. https://doi.org/10.1109/JSTARS.2016.2639043.
Tour, A., Thomson, K.P.B., Edwards, G., Brown, R.J., Brisco, B.G., 1994. Adaptation of the MIMICS backscattering model to the agricultural context-wheat and canola at L and C bands. IEEE Trans. Geosci. Rem. Sens. 32.
Touzi, R., Lapointe, M., Fobert, M.A., Nadelcu, S., Cote, S., 2023. Assessment and calibration of RCM compact-hybrid modes. IGARSS 2023 - 2023 IEEE International Geoscience and Remote Sensing Symposium. IEEE, pp. 7840–7843.
Ulaby, F.T., Long, D.G., Blackwell, W.J., Elachi, Charles, Fung, A.K., Chris, Ruf, et al., 2014. Microwave Radar and Radiometric Remote Sensing. The University of Michigan Press.
Ulaby, F.T., Long, D., 2014. Volume-scattering models and land observations. Microwave Radar and Radiometric Remote Sensing.
Verhoest, N.E.C., Lievens, H., Wagner, W., Álvarez-Mozos, J., Moran, M.S., Mattia, F., 2008. On the soil roughness parameterization problem in soil moisture retrieval of bare surfaces from synthetic aperture radar. Sensors 8, 4213–4248. https://doi.org/10.3390/s8074213.
Vermunt, P.C., Steele-Dunne, S.C., Khabbazan, S., Kumar, V., Judge, J., 2022. Towards understanding the influence of vertical water distribution on radar backscatter from vegetation using a multi-layer water cloud model. Remote Sens (Basel) 14. https://doi.org/10.3390/rs14163867.
Wang, H., Magagi, R., Goïta, K., Duguay, Y., Trudel, M., Muhuri, A., 2023b. Retrieval performances of different crop growth descriptors from full- and compact-polarimetric SAR decompositions. Remote Sens. Environ. 285. https://doi.org/10.1016/j.rse.2022.113381.
Wang, Y., Zhao, H., Fan, J., Wang, C., Ji, X., Jin, D., et al., 2023a. A review of earth's surface soil moisture retrieval models via remote sensing. Water (Switzerland) 15. https://doi.org/10.3390/w15213757.
Wang, L., Qu, J.J., 2009. Satellite remote sensing applications for surface soil moisture monitoring: a review. Front. Earth Sci. China 3, 237–247. https://doi.org/10.1007/s11707-009-0023-7.
Weis, T., Jagdhuber, T., Ramsauer, T., Low, A., Marzahn, P., 2024. RTM-based downscaling of medium resolution soil moisture using Sentinel-1 data over agricultural fields. IEEE J. Sel. Top. Appl. Earth Obs. Remote Sens. https://doi.org/10.1109/JSTARS.2024.3448625.
Wu, T.D., Chen, K.S., 2004. A reappraisal of the validity of the IEM model for backscattering from rough surfaces. IEEE Trans. Geosci. Rem. Sens. 42, 743–753. https://doi.org/10.1109/TGRS.2003.815405.
Yang, Z., Li, K., Shao, Y., Brisco, B., Liu, L., 2016. Estimation of paddy rice variables with a modified water cloud model and improved polarimetric decomposition using multi-temporal RADARSAT-2 images. Remote Sens (Basel) 8. https://doi.org/10.3390/rs8100878.
Zakharov, I., Kohlsmith, S., Hornung, J., Charbonneau, F., Bobby, P., Howell, M., 2024. Surface soil moisture estimation from time series of RADARSAT constellation mission compact polarimetric data for the identification of water-saturated areas. Remote Sens (Basel) 16. https://doi.org/10.3390/rs16142664.

Zhang, Y.-Y., Wu, Z.-S., 2016. Bistatic scattering characteristics of wheat and soybean by radiative transfer model in L band and C band. Prog. Electromagn. Res. B 67, 121–136.

Zhou, X., Wang, J., Shan, B., He, Y., 2025a. Soil moisture retrieval over soybean fields during growing season using polarimetric decomposition and time-series RCM data. Comput. Electron. Agric. 229. https://doi.org/10.1016/j.compag.2025.109935.

Zhou, X., Wang, J., Shan, B., He, Y., Xing, M., 2025b. Sensitivity of multi-frequency and multi-polarization SAR to soil moisture at different depths in agricultural regions. J. Hydrol. (Amst.) 660. https://doi.org/10.1016/j.jhydrol.2025.133513.

Zhou, X., Wang, J., 2023. Soil moisture retrieval over crop region using time-series high-resolution RCM data. In: International Geoscience and Remote Sensing Symposium (IGARSS), 2023– July. Institute of Electrical and Electronics Engineers Inc., pp. 3578–3581. https://doi.org/10.1109/IGARSS52108.2023.10281694